A Study on the Link Level Performance of Advanced Multicarrier Waveforms Under MIMO Wireless Communication Channels

Dan Zhang, Maximilian Matthé, Luciano Leonel Mendes, and Gerhard Fettweis

***Abstract*— This paper studies the link level performance of orthogonal frequency division multiplexing (OFDM) and four other advanced waveforms, namely, filtered OFDM (F-OFDM), universal-filtered OFDM (UF-OFDM), filter bank multicarrier (FBMC) and generalized frequency division multiplexing (GFDM). Compared to OFDM, the two filtered variants achieve lower out-of-band (OOB) emissions and can mostly preserve the conventional OFDM-based transceiver design. For the latter two non-orthogonal waveforms, this paper proposes a low complexity implementation of minimum mean square error equalization to jointly tackle the channel and waveform-induced interference. On this basis, the benefits of FBMC and GFDM can be exploited with complexity comparable to the former (quasi-)orthogonal waveforms. The observed benefits include lower peak-to-average power ratio (PAPR) and smaller frame error rate (FER) under challenging doubly dispersive multiple-input multiple-output (MIMO) fading channels. Additionally, linear filtering of FBMC offers an ultra-low OOB emission, while a good compromise in the usage of time and frequency resources can be achieved by circular filtering of GFDM. In the comparison of offset quadrature amplitude modulation (OQAM) versus QAM for non-orthogonal waveforms, OQAM can offer lower PAPR, while smaller FERs can be achieved by QAM in rich multipath fading channels.**

***Index Terms*— 5G, orthogonal and non-orthogonal waveforms, link level performance, MMSE equalization, MIMO.**

I. Introduction

FOR next generation communications systems, there is no doubt that providing higher data rates is one design goal. Beyond that, we are facing new requests [1]. For instance, Internet of things (IoT) requires wireless connection of tens of billions of devices, relying on simple signal processing and asynchronous multiple access. The whole idea of Tactile Internet [2] demands an ultra-low latency and/or ultra-high reliability. Areas with low population density are the final frontier for mobile communication. We shall provide an economically feasible wireless regional area network (WRAN) operation mode to deliver the service [3]. In order to serve all these diverse applications, the waveform adopted by the physical layer (PHY) plays an important role.

In the last decade, orthogonal frequency division multiplexing (OFDM) has evolved as a popular multicarrier scheme in different standards, including 3GPP LTE and WiFi families. Its orthogonality in the ideal situation permits one-tap frequency domain equalization under multipath fading channels and enables straightforward compatibility with multiple-input multiple-output (MIMO) techniques. However, with new and even more stringent requirements, OFDM faces its limitations, such as sensitivity to time-frequency misalignments, high out-of-band (OOB) emission, limited flexibility and high peak-to-average power ratio (PAPR) [4], [5]. To overcome these limitations, advanced alternatives have been intensively investigated in recent years, e.g., [6].

One group of proposals aims to improve OFDM while mostly keeping its orthogonality. Filtered OFDM (F-OFDM) [7] filters a set of contiguous subcarriers that form a subband and uses a cyclic prefix (CP) to avoid inter-symbol interference (ISI) introduced by the multipath channel. However, its filter tail spreads outside the duration of each OFDM block, which, without a sufficiently long CP, introduces inter-block interference (IBI).[1] To alleviate IBI, we can widen the bandwidth of the filter to shorten its impulse response in the time domain. This is equivalent to inserting one or several guard tones (GTs) between adjacent subbands. In universal-filtered OFDM (UF-OFDM), linear filtering is analogously applied on top of the subband [8]. To limit the potential IBI, it chooses shorter filters and switches from CP to zero padding (ZP) for accommodating the filter tail. However, shorter filter results in an inferior OOB emission performance. The high PAPR remains as a common problem for them.

Another group of waveforms, e.g., filter bank multicarrier (FBMC) [9] and generalized frequency division multiplexing (GFDM) [10], completely discards the orthogonality requirement of OFDM to achieve better temporal and spectral characteristics. Their common parts include: 1) filtering on a subcarrier basis, 2) permission of more than one data symbol per subcarrier, and 3) being subject to ISI and inter-carrier

Manuscript received March 16, 2016; revised November 2, 2016; accepted January 23, 2017. Date of publication March 13, 2017; date of current version April 7, 2017. This work was supported in part by the Federal Ministry of Education and Research within the programme "Twenty20–Partnership for Innovation" under contract 03ZZ0505B–"fast wireless," and in part by CNPq-Brasil and Finep/Funttel/Radiocommunication Reference Center under Grant No. 01.14.0231.00 hosted by Inatel. The associate editor coordinating the review of this paper and approving it for publication was A. Wyglinski

D. Zhang, M. Matthé, and G. Fettweis are with the Vodafone Chair Mobile Communication Systems, Technische Universität Dresden, 01069 Dresden, Germany (e-mail: dan.zhang@ifn.et.tu-dresden.de; maximilian.matthe@ifn.et.tu-dresden.de; fettweis@ifn.et.tu-dresden.de).

L. Mendes is with Instituto Nacional de Telecomunicações, Sta. Rita do Sapucai MG 37540-000, Brazil (e-mail: luciano@inatel.br).

Color versions of one or more of the figures in this paper are available online at http://ieeexplore.ieee.org.

Digital Object Identifier 10.1109/TWC.2017.2664820

[1] In this paper, one OFDM block in the discrete-time model consists of K samples plus the number of samples in the CP, where K is the total number of subcarriers. On this basis, we can distinguish the interference among symbols within one block, i.e., ISI, from that cross the blocks, i.e., IBI. The same definition applies for the other waveforms.

interference (ICI) arising from their non-orthogonality. With respect to 3), some works in the literature have suggested the adoption of offset quadrature amplitude modulation (OQAM) instead of QAM to achieve orthogonality in the real domain. However, complex-valued multipath channels can easily break such orthogonality, thereby the receiver still has to handle the ISI and ICI. The two waveforms also have several distinct features. FBMC adopts linear filtering to significantly reduce OOB emission for the sake of spectral efficiency and robustness against synchronization errors [9], [11]. On the other hand, the long filter length makes it more suitable for continuous rather than burst transmission, considering the usage efficiency of time resources. FBMC does not use a CP and can rely on the soft transition of its filter tail to combat multipath fading. In GFDM, a unique feature initially adopted by it is circular filtering. This ensures a block-based waveform with no filter tails, but at the cost of an increased OOB emission. GFDM does use a CP, but a single one can protect multiple data symbols for the sake of temporal efficiency.

Due to the self-introduced interference, non-orthogonal waveforms often require much increased receiver complexity, e.g., [12]–[14] and references therein. This situation even becomes more challenging in a MIMO system due to the additional inter-antenna interference (IAI). In this paper, we contribute an innovative way to perform minimum mean squared error (MMSE) equalization such that IAI, ISI and ICI can be jointly tackled with complexity in the same polynomial order as that of (quasi-)orthogonal waveforms.

The second main contribution of this paper is to study the link level performance of the above mentioned waveforms, including OOB emission, PAPR and coded frame error rate (FER) achieved by the linear MMSE receiver. Challenging channel conditions in terms of large delay spread and time-varying fading with imperfect synchronization and channel estimation are of particular interest. In the literature, several prior works aiming at waveform comparison are available. In [5], the authors conceptually suggested the applicable scenarios of OQAM-FBMC, filtered OFDM (F-OFDM), UF-OFDM and GFDM without performance evaluation. In [11], the authors mainly analyzed the robustness of waveforms under time- and frequency- misalignment and multi-user interference. The work in [15] addressed different techniques for reducing OOB emission in particular. The spectral efficiency of FBMC, OFDM and single-carrier frequency division multiple access (SC-FDMA) systems were compared in [4], where other waveform candidates and imperfect channel state information (CSI) were not considered. The authors of [16] compared performance of F-OFDM, UF-OFDM and OQAM-FBMC only under slow fading and nearly flat channels. In [17], the authors compared the PAPR and FER of OQAM-FBMC, GFDM, OFDM and SC-FDMA in the context of large-scale MIMO systems. However, equalization for different waveforms were not conducted under the same criterion and F-OFDM and UF-OFDM were not included. Even though a significant effort has been spent on waveform comparison, this is the first work, to our best knowledge, that provides comparison among all above mentioned waveforms in terms of OOB emission, PAPR and coded FER under realistic channel assumptions.

The remainder of this paper is organized as follows: Section II briefly describes each waveform, analyzes the modulation complexity, and compares the usage of time and frequency resources. Section III introduces the channel model and receiver design, mainly focusing on the derivation of a low complexity MMSE equalization scheme that can jointly resolve IAI, ICI and ISI for non-orthogonal waveforms using both QAM and OQAM. Section IV evaluates and compares the performance of the waveforms. Finally, conclusion and remarks are presented in Section V.

Notations: The letter j denotes $\sqrt{-1}$ and $\mathbf{I}_N$ represents the identity matrix of dimension N. $\mathbf{1}_{U,V}$ stands for an all-ones matrix of dimension $U \times V$. The cardinality of a discrete set $\mathcal{X}$ is denoted as $|\mathcal{X}|$. $I_v \cap I_{v+1}$ denotes the joint set of two sets I_v and I_{v+1}, while the relative complement of I_v in I_{v+1} can be written as $I_{v+1} \backslash I_v$. The operation $\langle a \rangle_n$ represents a modulo n. The distribution of a proper Gaussian random vector $\mathbf{x}$ with mean $\boldsymbol{\mu}$ and covariance matrix $\boldsymbol{\Sigma}$ is written as $\mathcal{CN}(\mathbf{x}; \boldsymbol{\mu}, \boldsymbol{\Sigma})$. The nth entry of $\mathbf{x}$ is denoted as $[\mathbf{x}]_n$ and $[\mathbf{X}]_{n,m}$ is the (n, m)th entry of the matrix $\mathbf{X}$. $[\mathbf{x}]_I$ is a subvector whose entries have indices belonging to the index set I. We denote the conjugate, transpose and conjugate transpose as $(\cdot)^*$, $(\cdot)^{\mathrm{T}}$ and $(\cdot)^{\mathrm{H}}$, respectively. The Kronecker and Hadamard product of two matrices are denoted by $\otimes$ and $\circ$, respectively.

II. Waveform Description

Consider a spatial multiplexing MIMO system equipped with N_{t} transmit and N_{r} receive antennas. Following bit-interleaved coded modulation, the message is coded, interleaved and mapped to a sequence of data symbols belonging to a given constellation set $\mathcal{X}$. This section introduces the waveforms that convey the data symbol sequence for further transmission over the air. To avoid over-complicated notations, we reuse variables that share the same meaning but possibly with different configurations for the waveforms. For instance, K represents the number of subcarriers, but it may have different values depending on the subcarrier spacing defined by each waveform. Under the same total bandwidth constraint, the signal in different waveforms will be presented in a discrete-time model obtained at the same sampling rate.

A. OFDM and Its Two Filtered Variants

Starting from OFDM, we assume that a set $\mathcal{K} \subset \{-\lceil \frac{K-1}{2} \rceil, \ldots, \lfloor \frac{K-1}{2} \rfloor\}$ of contiguous subcarriers out of the total K subcarriers is formed as a subband for data transmission.[2] To transmit the complete data symbol sequence, we need N_{s} OFDM blocks to form a frame. The discrete-time model of the sth OFDM block transmitted via the n_{t}th antenna is given as

$$x_{n_{\mathrm{t}}}^{[s]}[n] = \sum_{k \in \mathcal{K}} d_{n_{\mathrm{t}},k}^{[s]} e^{j \frac{2\pi k (n - L_{\mathrm{cp}})}{K}} \Omega_{K+L_{\mathrm{cp}}}[n], \quad \text{for} \quad n = 0, 1, \ldots, \tilde{K} - 1, \tag{1}$$

[2]In this paper, we mainly consider contiguous subcarrier allocation and the elements in $\mathcal{K}$ are sorted in an ascending order.

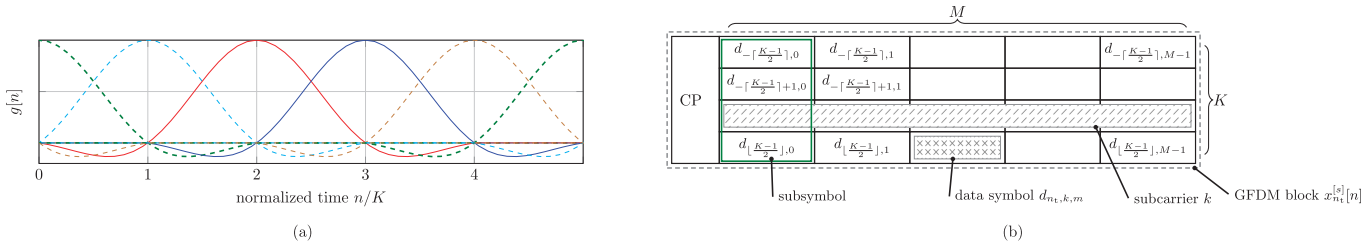

Fig. 1. Illustration of circular filtering in GFDM and its time-frequency grid.

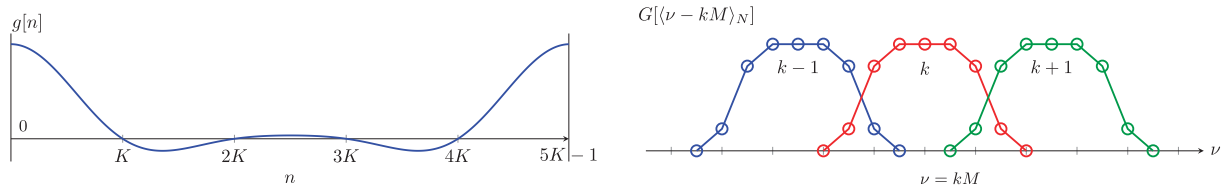

Fig. 2. Circular filter $g[n]$ is set to be a periodic RC function with roll-off factor $\alpha = 0.5$ and applied for the GFDM block with $M = 5$. With three consecutive subcarriers, the frequency domain expression of the signal is expressed in terms of the N-point DFT $G[\nu]$ of $g[n]$.

where $d_{n_t,k}^{[s]} \in \mathcal{X}$ is the data symbol carried by the kth subcarrier; $\tilde{K}$ equals K plus the CP length L_{cp} and the windowing function $\Omega_{K+L_{cp}}[n]$ yields 1 for any $n \in [0, K + L_{cp} - 1]$, otherwise it yields zero. The concatenation of such N_s OFDM blocks yields one frame

$$x_{n_t}[n] = \sum_{s=0}^{N_s-1} x_{n_t}^{[s]}[n - s\tilde{K}], \quad n = 0, 1, \ldots, N_s\tilde{K} - 1. \quad (2)$$

On the basis of (2), F-OFDM applies a linear filter $f[n]$ with length L_f to limit the energy leakage outside the given subband. In equation, we have

$$x_{n_t}[n] = \left[\sum_{s=0}^{N_s-1} \sum_{k \in \mathcal{K}} d_{n_t,k}^{[s]} e^{j\frac{2\pi k(n-L_{cp}-s\tilde{K})}{K}} \Omega_{K+L_{cp}}[n - s\tilde{K}] \right] * \left[f[n] e^{j\frac{2\pi k_c n}{K}} \right], \quad (3)$$

for $n = 0, 1, \ldots, N_s\tilde{K} + L_f - 2$, where k_c is the center frequency of the subband normalized by the sampling rate. By having different configurations of L_{cp} and $\tilde{K}$, the above expression is also usable for describing UF-OFDM. Since UF-OFDM uses ZP instead of CP, L_{cp} becomes zero and $\tilde{K}$ equals $K + L_{zp}$, where L_{zp} is the number of zeros appended to the block tail. Aiming at the same block duration, L_{zp} is set to equal L_{cp} by default in this paper. Another key difference between F-OFDM and UF-OFDM lies in the choice of $f[n]$. Hanning windowed sinc-function is suggested for F-OFDM [18], while UF-OFDM typically adopts a Dolph-Chebyshev filter [19]. The typical length of the former is $K/2 + 1$ but its most energy is contained by L_{cp} samples. The latter is chosen to be confined within the duration of ZP, thereby being more compact than the former. The good frequency localization of both filters is usable for limiting the OOB emission, but linear filtering also introduces IBI, particularly in combination with a highly frequency-selective fading channel. For more details on F- and UF-OFDM, we refer the readers to [7], [18], [20].

B. GFDM

GFDM is a non-orthogonal multicarrier waveform. Each subcarrier can carry M data symbols that are temporally equally spaced and circularly filtered by a filter $g[n]$, see Fig. 1(a). Fig. 1(b) illustrates one GFDM block in the time-frequency grid. In equation, the sth GFDM block can be written as

$$x_{n_t}^{[s]}[n] = \sum_{k \in \mathcal{K}} \sum_{m=0}^{M-1} d_{n_t,k,m}^{[s]} g[\langle n - mK - L_{cp} \rangle_N] e^{j\frac{2\pi(n-L_{cp})k}{K}} \times \Omega_{N+L_{cp}}[n] \quad (4)$$

for $n = 0, 1, \ldots, N + L_{cp} - 1$, where N equals MK, and $d_{n_t,k,m}^{[s]} \in \mathcal{X}$ is the mth data symbol that is on the kth subcarrier and via the transmit antenna n_t. Assume N_s such GFDM blocks are needed to convey the complete data symbol sequence, yielding one GFDM frame

$$x_{n_t}[n] = \sum_{s=0}^{N_s-1} x_{n_t}^{[s]}[n - sN - sL_{cp}] \quad (5)$$

for $n = 0, 1, \ldots, N_s(N + L_{cp}) - 1$.

For later use, here we also examine the frequency domain expression of each GFDM block. In the literature, e.g., [10], a typical choice of $g[n]$ is the periodic raised cosine (RC) filter with a given roll-off factor α, see Fig. 2. Let us denote the N-point DFT of $g[n]$ as $G[\nu]$ for $\nu = 0, 1, \ldots, N - 1$. The N-point DFT of $x_{n_t}^{[s]}[n]$ after CP removal can be written as

$$X_{n_t}^{[s]}[\nu] = \sum_{k \in \mathcal{K}} G[\langle \nu - kM \rangle_N] D_{n_t,k,u=\langle \nu \rangle_M}^{[s]}, \quad \text{for } \nu = 0, 1, \ldots, N - 1, \quad (6)$$

where $D_{n_t,k,u}^{[s]}$ is effectively the uth harmonic of the M data symbols carried by the subcarrier k

$$D_{n_t,k,u}^{[s]} = \sum_{m=0}^{M-1} d_{n_t,k,m}^{[s]} e^{-j\frac{2\pi mu}{M}}, \quad \text{for } u = 0, 1, \ldots, M - 1. \quad (7)$$

From (6) and also as illustrated in Fig. 2, an alternative view of GFDM modulation can be a process of: 1) M-point DFT spreading for the M data symbols per subcarrier, 2) repeatedly modulating the M harmonics onto the N frequency bins and 3) weighting them by the window $G[\nu]$ with appropriate circular shifts to ensure their correct positions in the spectrum. If the window $G[\nu]$ is rectangular with M non-zero coefficients, $X_{n_\mathrm{t}}^{[s]}[\nu]$ is equivalent to DFT spreading OFDM (DFT-s-OFDM). DFT spreading introduces ISI and a non-rectangular window $G[\nu]$ with more than M non-zero coefficients retains ICI. We shall note that interference, different to background noise, carries data information. Through the ISI and ICI of GFDM, the information of each data symbol is effectively contained by more than M frequency domain observations. This offers an opportunity to exploit the frequency selectivity of the multipath fading channel for data transmission.

C. FBMC

In this part, we introduce FBMC with the use of OQAM, which is a common combination suggested in the literature. By further linking FBMC with GFDM, we can reach to an alternative expression in terms of OQAM-GFDM. In a general sense, such a link enables the mutual use of techniques respectively developed for GFDM and FBMC.

Formally, one OQAM-FBMC block, that consists of K subcarriers and uses the filter of length L_f to respectively carry the real and imaginary parts of a complex-valued data symbol $d_{n_\mathrm{t},k,m} = d_{n_\mathrm{t},k,m}^{\mathrm{Re}} + j d_{n_\mathrm{t},k,m}^{\mathrm{Re}} \in \mathcal{X}$ with the time spacing of $K/2$ samples, can be expressed as

$$x_{n_\mathrm{t}}[n] = \sum_{k\in\mathcal{K}} \sum_{m=0}^{M-1} j^k e^{j\frac{2\pi k}{K}\left(n-\frac{L_\mathrm{f}-1}{2}\right)} \times \left\{ d_{n_\mathrm{t},k,m}^{\mathrm{Re}} f\left[n - mK\right] + j d_{n_\mathrm{t},k,m}^{\mathrm{Im}} f\left[n - mK - K/2\right] \right\} \quad (8)$$

for $n = 0, 1, \ldots, MK - K/2 + L_\mathrm{f} - 1$. In this paper, we choose the PHYDYAS filter [9] of length $L_\mathrm{f} = 4K$ and it is centered at $L_\mathrm{f}/2$. Considering such a long filter, one FBMC block per frame is a sensible choice for an efficient use of time resources. Then, the block expression in (8) also represents the frame, thereby omitting the superscript block index $(\cdot)^{[s]}$. If switching to a QAM scheme, $d_{n_\mathrm{t},k,m}^{\mathrm{Re}}$ and $d_{n_\mathrm{t},k,m}^{\mathrm{Im}}$ in (8) shall be respectively replaced by $d_{n_\mathrm{t},k,m}$ and 0, and also j^k is negligible. More details about FBMC can be found in [9], [21] and references therein.

Next, aiming at the connection between FBMC and GFDM, let us recall the circular filtering of GFDM as illustrated in Fig. 1(b). Arbitrarily picking one wave, the other $(M-1)$ waves can be generated via circular shifts by integer multiples of K samples. In the context of GFDM, the overall M waves are used for data transmission. With respect to the solid waves in the middle, their energy is consecutively confined within $4K$ out of the overall MK samples. Given this view, they can also be interpreted as the outcomes of linear filtering with equal temporal shifts. Under this identification, we can effectively realize linear filtering of FBMC by GFDM through: 1) choosing a time limited filter, e.g., the first solid wave peaked at $n = 2K$ of Fig. 1(b); 2) zero padding to reach the same length as the block; 3) circularly shifting it to form the equally temporally spaced waves; and 4) turning off those that exhibit the tail biting effect due to circular filtering, e.g., dashed waves in Fig. 1(b). Practicing this general concept for OQAM-FBMC given in (8), we shall start from appending zeros to the tail of the PHYDYAS filter $f[n]$ of length $4K$ such that the filter length equals $\tilde{N} = (M+4)K$, which is the smallest integer multiple of K that is greater than the block length $MK + \frac{7}{2}K$. Here, due to the $K/2$-sample shift introduced by OQAM, the filter after zero padding is $K/2$ samples longer than the initial block length to achieve an integer multiple of K. On this basis, we circularly shift the zero-padded filter by $2K$ samples towards left to construct a circular filter $\tilde{g}[n]$ of length $\tilde{N}$ and peaked at the zero point, analogous to the first dashed green wave in Fig. 1(b). In terms of $\tilde{g}[n]$, the combination of OQAM with GFDM yields the following alternative expression of (8)

$$\tilde{x}_{n_\mathrm{t}}[n] = \sum_{k\in\mathcal{K}} \sum_{m=0}^{\tilde{M}-1} j^k e^{j\frac{2\pi k\left(n-\frac{L_\mathrm{f}-1}{2}\right)}{K}} \times \left\{ a_{n_\mathrm{t},k,2m}\tilde{g}\left[\langle n - mK\rangle_{\tilde{N}}\right] + j a_{n_\mathrm{t},k,2m+1}\tilde{g}\left[\left\langle n - mK - \frac{K}{2}\right\rangle_{\tilde{N}}\right]\right\} \quad (9)$$

with $\tilde{M} = M + 4$ and the new real-valued symbol sequences $a_{n_\mathrm{t},k,m}$ are defined as

$$\begin{cases} a_{n_\mathrm{t},k,2m} = 0 \\ a_{n_\mathrm{t},k,2m+1} = 0 \end{cases} \quad m \in \{0, 1, \tilde{M}-2, \tilde{M}-1\}$$
$$\begin{cases} a_{n_\mathrm{t},k,2m} = d_{n_\mathrm{t},k,m-2}^{\mathrm{Re}} \\ a_{n_\mathrm{t},k,2m+1} = d_{n_\mathrm{t},k,m-2}^{\mathrm{Im}} \end{cases} \quad m = 2, \ldots, \tilde{M}-3. \quad (10)$$

In above, the first and last two real-valued symbols are set to zero for avoiding the tail biting effect of circular filtering, and also the CP of GFDM is omitted. Compared to (8), we can also interpret (9) as the outcome of letting FBMC adopt circular filtering, e.g., [22], [23].

Performing $\tilde{N}$-point DFT of $\tilde{x}_{n_\mathrm{t}}[n]$ for $n = 0, 1, \ldots, \tilde{N}-1$, the outcome is

$$\tilde{X}_{n_\mathrm{t}}[\nu] = \sum_{k\in\mathcal{K}} \tilde{G}\left[\left\langle \nu - \tilde{M}k\right\rangle_{\tilde{N}}\right] e^{-j\frac{2\pi k}{K}\frac{L_\mathrm{f}-1}{2}} j^k A_{n_\mathrm{t},k,u=\langle\nu\rangle_{2\tilde{M}}}, \quad (11)$$

where $\tilde{G}[\nu]$ is the $\tilde{N}$-point DFT of $\tilde{g}[n]$ and $A_{n_\mathrm{t},k,u}$ for $u = 0, 1, \ldots, 2\tilde{M}-1$ is given as

$$A_{n_\mathrm{t},k,u} = \sum_{m=0}^{\tilde{M}-1} a_{n_\mathrm{t},k,2m} e^{-j2\pi\frac{2mu}{2\tilde{M}}} + (-1)^k j a_{n_\mathrm{t},k,2m+1} e^{-j2\pi\frac{(2m+1)u}{2\tilde{M}}}. \quad (12)$$

Analogous to (6), the data symbols are not directly modulated onto the frequency bin ν. Before that, they are precoded by means of DFT and then weighted by the window $\tilde{G}[\nu]$ with appropriate shifts. It is important to note that

TABLE I

FRAME PARAMETERIZATION AND MODULATION COMPLEXITY

* The parameters, i.e., K, $\mathcal{K}$, T, N_s, M and L_cp, are given to derive the configuration of each waveform based on the relation indicated in the table.
* For OFDM, L_f equals zero. For FBMC, the PHYDYAS filter has length of $L_\mathrm{f} = 4K$ [9]. For UF-OFDM, L_zp is set to equal L_cp.
* Low-complexity implementations for UF-OFDM, GFDM and OQAM-FBMC are given in [19], [25], [26], respectively.
* $O(1)$ represents the arithmetic complexity per multiplication.

Waveform	Nr. dat. symbs per subcar.	Nr. blks per frame	Nr. subcar. per blk.	Nr. act. subcar.	Subcar. spacing.	Sampling rate	Frame length	Arithmetic complexity per data symb.
(F/UF-)OFDM	–	N_s	K	$\lvert\mathcal{K}\rvert$	$1/T$	K/T	$\frac{(K+L_\mathrm{cp})N_\mathrm{s}+L_\mathrm{f}-1}{K}T$	$O\left(\frac{K}{\lvert\mathcal{K}\rvert}\log K + \frac{KL_\mathrm{f}}{\lvert\mathcal{K}\rvert}\right)$
GFDM-I	N_s	1	K	$\lvert\mathcal{K}\rvert$	$1/T$	K/T	$(N_\mathrm{s}+\frac{L_\mathrm{cp}}{K})T$	$O\left(\frac{K}{\lvert\mathcal{K}\rvert}\log K + \frac{KM}{\lvert\mathcal{K}\rvert}\right)$
FBMC-I	N_s	1	K	$\lvert\mathcal{K}\rvert$	$1/T$	K/T	$(N_\mathrm{s}+\frac{7}{2})T$	$O\left(\frac{K}{\lvert\mathcal{K}\rvert}\log K + \frac{4K}{\lvert\mathcal{K}\rvert}\right)$
GFDM-II	M	N_s	K/M	$\lvert\mathcal{K}\rvert/M$	M/T	K/T	$\frac{(K+L_\mathrm{cp})N_\mathrm{s}}{K}T$	$O\left(\frac{K}{\lvert\mathcal{K}\rvert}\log(K/M) + \frac{KM}{\lvert\mathcal{K}\rvert}\right)$
FBMC-II	$N_\mathrm{s}M$	1	K/M	$\lvert\mathcal{K}\rvert/M$	M/T	K/T	$(N_\mathrm{s}+\frac{7}{2M})T$	$O\left(\frac{K}{\lvert\mathcal{K}\rvert}\log(K/M) + \frac{4K}{\lvert\mathcal{K}\rvert}\right)$

$\{a_{n_\mathrm{t},k,2m}, a_{n_\mathrm{t},k,2m+1}\}$ in (12) are real-valued. Their $2\tilde{M}$-point DFTs have the following property

$$A_{n_\mathrm{t},k,u} = A^*_{n_\mathrm{t},k,\tilde{M}-u} \quad \text{and } A_{n_\mathrm{t},k,u+\tilde{M}} = A^*_{n_\mathrm{t},k,2\tilde{M}-u} \tag{13}$$

for any $u \in \{0, 1, \ldots, \tilde{M}-1\}$. Taking $u = 2$ as an example, $A_{n_\mathrm{t},k,u=2}$ will be contained in $\tilde{X}_{n_\mathrm{t}}[\nu]$ with $\langle\nu\rangle_{2\tilde{M}} = 2$ and $\tilde{X}^*_{n_\mathrm{t}}[\nu]$ with $\langle\nu\rangle_{2\tilde{M}} = \tilde{M}-2$. Since the filter shall have a good frequency localization, the main span of the window $\tilde{G}[\nu]$ is typically smaller than $2\tilde{M}$, i.e., ICI only from the adjacent subcarriers. This implies after windowing $A_{n_\mathrm{t},k,u=2}$ will be maximumly conveyed by two frequency bins with spacing $\tilde{M}-4$. Among all feasible values of u, the maximum spacing is $\tilde{M}$ and it is attained by $u = 0$. In contrast, for any u, QAM-GFDM as given in (6) always modulates $\{D_{n_\mathrm{t},k,u}\}$ onto the frequency bins with equal spacing M. Therefore, when M and $\tilde{M}$ have comparable values and the spectral spacing between frequency bins is similar, we expect QAM superior to OQAM in terms of exploiting the frequency selectivity of the multipath channel for data transmission.

D. Short Summary

To conclude this section, Table I lists the parameters relevant to individual waveforms. Specifically, the configuration of the baseline CP-OFDM is characterized by: the number K of subcarriers, the duration T (in a time unit) of one OFDM block without CP, the CP length L_cp, the set $\mathcal{K}$ of active subcarriers and the number N_s of CP-OFDM blocks per frame. In terms of the listed parameters, the configurations of the other waveforms are derived under the constraint that each frame uses the same bandwidth and carries the same number of data symbols.[3] Since GFDM and FBMC have one additional degree of freedom in time, two representative configurations for them are considered here. For the type-I configuration, we configure them to have the same number of subcarriers and subcarrier spacing as the baseline OFDM. In the time domain, each subcarrier carries N_s data symbols with equal temporal spacing T, yielding one block per frame. The type-II configuration increases the subcarrier spacing by M times. Under the constraint of identical spectrum, the total number of subcarriers and also the active ones are accordingly reduced by M times. As GFDM is a block-based waveform, we let each GFDM-II block carry M data symbols per subcarrier and use N_s GFDM-II blocks to form a frame. In this case, GFDM-II and the baseline OFDM have the same block length and carry the same number of data symbols per block. For FBMC-II, we still keep one block per frame for the sake of temporal efficiency, implying $N_\mathrm{s}M$ data symbols per subcarrier.

Based on the above configurations, we can calculate the frame length of each waveform. Circular filtering of GFDM makes it more compact in time. One CP to protect N_s data symbols per subcarrier in the type-I case yields the shortest frame length among the waveforms. GFDM-II and the baseline OFDM have the second shortest frame length. Due to linear rather than circular filtering, F-OFDM, UF-OFDM and especially FBMC all require additional time resource to accommodate the filter tail. Regarding the arithmetic complexity of modulating each waveform, the minimum one is achieved by the baseline OFDM and it arises from the K-point DFT operation, i.e., $O(\frac{K}{\lvert\mathcal{K}\rvert}\log K)$ per data symbol. The other waveforms also need such DFT operations plus additional ones due to filtering.

III. CHANNEL MODEL AND RECEIVER DESIGN

Consider a multipath Rayleigh fading MIMO channel. Even though real channels are continuously time-varying, it is a common practice for the receiver to assume that the channel impulse response (CIR) remains constant during the transmission of each block. This assumption is also the premise for CP-OFDM being orthogonal after transmitting through the channel. Therefore, we ignore the time-varying nature of the CIR in this part for the receiver design. However, continuously time-varying channel models will be used for performance evaluation in Section IV.

With respect to the channel between the transceiver antenna pair $(n_\mathrm{t}, n_\mathrm{r})$, the discrete-time model of its CIR, consisting of L_h delay paths, is expressed as

$$h_{n_\mathrm{r},n_\mathrm{t}}[n] = \sum_{\upsilon=0}^{L_\mathrm{h}-1} h_{\upsilon,n_\mathrm{r},n_\mathrm{t}}\delta[n-\upsilon], \tag{14}$$

where $h_{\upsilon,n_\mathrm{r},n_\mathrm{t}}$ is the channel coefficient of the path υ and $\delta[\cdot]$ is the Kronecker delta function. Transmitting the signal

[3]Due to different choices of filter, it is difficult to achieve the same frame duration without violating the bandwidth constraint. Considering the strict regulation on the spectrum, identical bandwidth is our primary constraint.

$x_{n_\mathrm{t}}[n]$ over such channel, the observation $r_{n_\mathrm{r}}[n]$ at the receive antenna n_r is expressed as

$$r_{n_\mathrm{r}}[n] = \sum_{n_\mathrm{t}=1}^{N_\mathrm{t}} x_{n_\mathrm{t}}[n] * h_{n_\mathrm{r},n_\mathrm{t}}[n] + w_{n_\mathrm{r}}[n], \tag{15}$$

where the spatially and temporally white proper Gaussian noise $w_{n_\mathrm{r}}[n]$ has zero mean and variance N_0. In order to recover the transmitted message based on $r_{n_\mathrm{r}}[n]$, the main functional units of baseband signal processing include synchronization/channel estimation, equalization/detection and decoding. In the data-aided context, the synchronization and channel estimation algorithms based on the use of pre-/mid-/post-ambles, e.g., in WiFi families and LTE uplink, can be versatile to the waveforms. Switching to the pilot-based cases such as in the LTE downlink, the non-orthogonal waveforms will face the situation that the pilot observations are polluted by the unknown data symbols. This challenges the design of synchronization and channel estimation. One potential solution is to pre-cancel the interaction between data and pilot symbols already at the transmitter. On this basis, the receiver can again resort to the clean pilot observations for synchronization and channel estimation, analogous to the orthogonal case. Equipped with the synchronized received signal and channel estimates, the subsequent step is coherent equalization and detection. Namely, the equalizer treats the discrete data symbols as continuous random variables and estimates them given the received signals by following certain criterion.[4] Based on the estimates of the data symbols plus their estimated error variances attained by the equalizer, a soft detector commonly resorts to a Gaussian model and bases on the modulation rule to generate the soft information for each code bit, e.g., [26]. The final decoding unit depends on the adopted coding scheme.

From the above brief overview of the receiver, we notice that the equalization unit is inevitably waveform-dependent. Therefore, we focus on its design in this section and leave its performance evaluation in combination with the other functional units to the next section. Specifically, we follow the MMSE criterion to jointly resolve the channel- and waveform-induced (if present) interference. Since they are coupled together in the received signals, such joint equalization is expected to outperform those that handle the interference from the channel and waveform in two separated and non-interactive steps. Furthermore, the presented derivation of MMSE equalization assumes the output of the synchronization and channel estimation unit is perfect. In practice, any mismatch due to the synchronization and channel estimation errors can be treated as an additional noise that distorts data transmission.

The ensuing part starts from OFDM and its two variants. For them, the IAI from the MIMO channel is the main concern of the MMSE equalizer. Proceeding to the non-orthogonal GFDM and FBMC, our contribution is a low complexity implementation of MMSE equalization to jointly tackle not only the IAI, but also the ISI and ICI caused by the waveform.

[4]It is possible to skip equalization and directly perform detection, which means a mapping from the received samples to a sequence of points in the discrete constellation set. However, the required complexity grows exponentially with the number of data streams in superimposition. Therefore, equalization is often needed to first separate the data streams before considering the constellation constraint.

A. MMSE Equalization for OFDM

When the CP of each OFDM block is longer than the maximum delay length L_h of the channel, it fulfills two roles: 1) to preserve the orthogonality and 2) to prevent IBI after transmission over the multipath fading channel. Ignoring the initial L_cp received samples of each block, linear convolution with the CIR as given in (15) becomes equivalent to circular convolution with respect to individual OFDM blocks without CPs. Circular convolution in the time domain boils down to multiplication in the DFT domain, permitting frequency domain MMSE equalization to resolve the IAI on a subcarrier basis. Since the derivation is straightforward by following [27, Theorem 12.1], here we skip the details. One remark is worth noting. MMSE equalization is conditionally biased towards the a-priori distribution of data symbols, which are typically modeled as Gaussians with zero mean and variance equal to the energy per data symbol denoted as E_s. Such bias needs to be compensated before detection. This requires not only the MMSE estimates of the data symbols but also the error variances [26].

B. MMSE Equalization for F-OFDM

Comparing to OFDM, F-OFDM has one additional filtering at the transmitter. One direct solution is to consider the filter $f[n]$ as a part of the channel. However, with the filter suggested for F-OFDM, the filtered response of a highly frequency-selective channel can have length much longer than CP. The resulting IBI will then compromise the performance of any block-based equalization schemes, particularly at high signal-to-noise ratios (SNRs). To tackle this issue, the authors of [18] suggested matched filtering $f^*[-n]$ at the receiver followed by block-based MMSE equalization of the conventional CP-OFDM, which uses $f[n]*h_{n_\mathrm{r},n_\mathrm{t}}[n]*f^*[-n]$ as the effective CIR. The rationale behind this design can be understood by viewing the received F-OFDM signal as the outcome of two steps: 1) linearly convolving the regular CP-OFDM with the channel $h_{n_\mathrm{r},n_\mathrm{t}}[n]$ and 2) filtering on top of it to limit the OOB emission. Here, the order of the channel $h_{n_\mathrm{r},n_\mathrm{t}}[n]$ and the filter $f[n]$ is interchangeable because they are linear filters. Evidently, the MMSE equalizer of the regular CP-OFDM works with the samples at the output of step 1). However, the additional filtering in the step 2) introduces non-negligible interference among the samples, hindering its straightforward use. To mitigate the negative impact of filtering, the matched filter $f^*[-n]$ by definition yields the maximum SNR, where the output of step 1) is the signal of interest in this case. Given that interference among samples still exists, matched filtering is an effective approach when the interference is smaller than the background noise. We shall also note that matched filtering will color the noise, but the noise correlation is typically ignored for the sake of complexity.

C. MMSE Equalization for UF-OFDM

The key feature of UF-OFDM is to use ZP instead of CP such that the channel-induced energy leakage to the

subsequent block is reduced. Additionally, the length of the filter suggested for UF-OFDM is shorter than that of F-OFDM. For these two reasons, here we are able to directly combine the filter of UF-OFDM with the channel and skip matched filtering at the receiver. Then, MMSE equalization of UF-OFDM becomes equivalent to that of ZP-OFDM. By further applying overlap-and-add [28], the orthogonality achieved by CP-OFDM can be easily restored for ZP-OFDM, permitting MMSE equalization on a subcarrier basis. In fact, the baseline demodulation introduced in the literature, e.g. [20], for UF-OFDM exactly follows this line. It is noted that the overlap-and-add process introduces additional noise to the first L_{zp} received samples of each UF-OFDM block. As a result, the noise samples in the frequency domain associated to different subcarriers become correlated and also their variances are increased by the factor $(1 + L_{\mathrm{zp}}/K)$.

D. MMSE Equalization for GFDM

Similar to OFDM, GFDM adopts CP to combat multipath fading channels by converting linear convolution to circular convolution. With the respect to the channel model (14), we can then perform MMSE equalization for each received GFDM block without suffering from IBI. With respect to the sth GFDM block without CP, the channel input-output relation can be formed as

$$\begin{aligned} r_{n_{\mathrm{r}}}^{[s]}[n] &= r_{n_{\mathrm{r}}}[n + sN + sL_{\mathrm{cp}} + L_{\mathrm{cp}}] \\ &= \sum_{n_{\mathrm{t}}=1}^{N_{\mathrm{t}}} h_{n_{\mathrm{r}},n_{\mathrm{t}}}[n] \circledast x_{n_{\mathrm{t}}}^{[s]}[n + L_{\mathrm{cp}}] + w_{n_{\mathrm{r}}}^{[s]}[n] \end{aligned} \quad (16)$$

for $n = 0, 1, \ldots, N-1$ and with $w_{n_{\mathrm{r}}}^{[s]}[n] = w_{n_{\mathrm{r}}}[n + sN + sL_{\mathrm{cp}} + L_{\mathrm{cp}}]$ and $N = MK$. Performing N-point DFT on both sides of (16) and also given the frequency domain expression of $x_{n_{\mathrm{t}}}^{[s]}[n]$ in (6), we can reach to

$$\begin{aligned} R_{n_{\mathrm{r}}}^{[s]}[\nu] = &\sum_{n_{\mathrm{t}}=1}^{N_{\mathrm{t}}} H_{n_{\mathrm{r}},n_{\mathrm{t}}}[\nu] \sum_{k\in\mathcal{K}} G[\langle \nu - kM\rangle_N] D_{n_{\mathrm{t}},k,u=\langle\nu\rangle_M}^{[s]} \\ &+ W_{n_{\mathrm{r}}}^{[s]}[\nu], \end{aligned} \quad (17)$$

where $R_{n_{\mathrm{r}}}^{[s]}[\nu]$, $H_{n_{\mathrm{r}},n_{\mathrm{t}}}[\nu]$, and $W_{n_{\mathrm{r}}}^{[s]}[\nu]$ are respectively the outcomes of N-point DFTs of $r_{n_{\mathrm{r}}}^{[s]}[n]$, $h_{n_{\mathrm{r}},n_{\mathrm{t}}}[n]$, and $w_{n_{\mathrm{r}}}^{[s]}[n]$. Given the one-to-one linear mapping in (7), we can first perform MMSE estimation of $\{D_{n_{\mathrm{t}},k,u}^{[s]}\}$ based on (17) and then generate the MMSE estimates of $\{d_{n_{\mathrm{t}},k,u}^{[s]}\}$ by means of M-point IDFT. Unlike to directly estimate $\{d_{n_{\mathrm{t}},k,m}^{[s]}\}$, we only need to deal with the IAI and ICI appeared in (17) and ISI is no longer a concern here. We further note that M-point DFT effectively represents an orthogonal transform. Under the common assumption that the data symbols carried by each subcarrier are modeled as i.i.d. Gaussian random variables[5] for MMSE equalization, $\{D_{n_{\mathrm{t}},k,u}^{[s]}\}$ remains to be i.i.d. Gaussian random variables under such orthogonal transform. Due to the mutual independence and based on (17), MMSE estimation of $D_{n_{\mathrm{t}},k,u}^{[s]}$ for a given $u \in \{0, 1, \ldots, M-1\}$ will only rely on the observation and CSI associated to the frequency bins satisfying $\langle\nu\rangle_M = u$. Therefore, we introduce $\mathbf{R}_u^{[s]} \in \mathbb{C}^{N_{\mathrm{r}}K\times 1}$, $\mathbf{H}_u \in \mathbb{C}^{N_{\mathrm{r}}K\times N_{\mathrm{t}}}$ and $\mathbf{W}_u^{[s]} \in \mathbb{C}^{N_{\mathrm{r}}K\times 1}$ to respectively capture the observation, CSI and the noise associated to these frequency bins, namely

$$\begin{aligned} [\mathbf{R}_u^{[s]}]_{n_{\mathrm{r}}+\kappa N_{\mathrm{r}}} &\triangleq R_{n_{\mathrm{r}}}^{[s]}[\nu = \langle\kappa' M + u\rangle_N] \\ [\mathbf{H}_u]_{n_{\mathrm{r}}+\kappa N_{\mathrm{r}},n_{\mathrm{t}}} &\triangleq H_{n_{\mathrm{r}},n_{\mathrm{t}}}[\nu = \langle\kappa' M + u\rangle_N] \\ [\mathbf{W}_u^{[s]}]_{n_{\mathrm{r}}+\kappa N_{\mathrm{r}}} &\triangleq W_{n_{\mathrm{r}}}^{[s]}[\nu = \langle\kappa' M + u\rangle_N] \end{aligned}$$

for $\kappa = 0, \ldots, K-1$ and $\kappa' = \kappa - \lceil\frac{K-1}{2}\rceil$. And also, we use the matrix $\mathbf{G}_u \in \mathbb{C}^{K\times|\mathcal{K}|}$ to denote $|\mathcal{K}|$ column vectors where each corresponds to the K samples of $G[\langle\nu - kM\rangle_N]$ attained at $\nu = \langle\kappa' M + u\rangle_N$ for $\kappa' = -\lceil\frac{K-1}{2}\rceil, \ldots, \lfloor\frac{K-1}{2}\rfloor$ and $k \in \mathcal{K}$. For compactly denoting $\{D_{n_{\mathrm{t}},k,u}\}_{n_{\mathrm{t}},k}$, we first collect the N_{t} elements with identical k, and then stack them one after another in an ascending order of $k \in \mathcal{K}$ to form a column vector $\mathbf{D}_u^{[s]} \in \mathbb{C}^{N_{\mathrm{t}}|\mathcal{K}|\times 1}$. Using the above introduced notation, the equation (17) for all frequency bins can be grouped and compactly written as

$$\mathbf{R}_u^{[s]} = \left[\left(\mathbf{G}_u \otimes \mathbf{1}_{N_{\mathrm{r}},N_{\mathrm{t}}}\right) \circ \left(\mathbf{1}_{1,|\mathcal{K}|} \otimes \mathbf{H}_u\right)\right] \mathbf{D}_u^{[s]} + \mathbf{W}_u^{[s]} \quad (18)$$

for $u = 0, 1, \ldots, M-1$. On this basis, MMSE estimation for $\mathbf{D}_u^{[s]}$ can be executed simultaneously for different u. This is an important feature for supporting high-level parallelism in implementation. For each possible u, the complexity depends on the structure of the matrix $[(\mathbf{G}_u \otimes \mathbf{1}_{N_{\mathrm{r}},N_{\mathrm{t}}}) \circ (\mathbf{1}_{1,|\mathcal{K}|} \otimes \mathbf{H}_u)]$. First, the matrix may contain all-zero rows as not all frequency bins carry useful information. Such rows and the corresponding entries in $\mathbf{R}_u^{[s]}$ can be safely deleted to reduce the size of the linear system (18). Next, considering the general objective of choosing the circular filter $g[n]$ is to ensure good frequency localization, the main span of $G[\nu]$ is often smaller than $2M$, e.g., in Fig. 2. Then, the matrix after removing all-zero rows generally has two structures, depending on u. The first one applies for the ICI free case, e.g., $u = \langle\nu = k'M\rangle_M = 0$ in Fig. 2. The matrix equals the direct sum of matrices of dimension $N_{\mathrm{r}} \times N_{\mathrm{t}}$. In this case, the complexity is identical to the OFDM case, i.e., performing MMSE equalization to resolve IAI on each frequency bin. The second one applies for the ICI case, e.g., for $u = \langle\nu = k'M + 2\rangle_M = 2$ in Fig. 2. Under the condition $|\mathcal{K}| < K$ (e.g., the unused guard or DC subcarrier), we effectively have a tall band matrix whose upper and lower bandwidth equal $2N_{\mathrm{t}}$ and $2N_{\mathrm{r}}$, respectively. For such a matrix, we resort to the Markov chain based approach presented in Appendix for MMSE estimation. The required complexity $O(N_{\mathrm{r}}(2N_{\mathrm{t}})^2 + (2N_{\mathrm{t}})^3)$ per subcarrier is still comparable to OFDM and also there exists an implementation architecture supporting high-level parallelism.

Equipped with the MMSE estimates $\{\hat{D}_{n_{\mathrm{t}},k,u}^{[s]}\}$, we can then construct the MMSE estimate of individual data symbols by

[5]For data symbols carried by the same subcarrier, they are experiencing the same channel condition in the frequency domain. Therefore, it is natural to assume the identical power allocation. Among different subcarriers, it is possible to have adaptive power allocation. However, for notation simplicity, we assume identical power allocation cross subcarriers as well.

taking M-point IDFT

$$\hat{d}^{[s]}_{n_\mathrm{t},k,m} = \frac{1}{M}\sum_{u=0}^{M-1} \hat{D}^{[s]}_{n_\mathrm{t},k,u} e^{j\frac{2\pi um}{M}}, \tag{19}$$

while the knowledge of the error variance of the MMSE estimate $\hat{D}^{[s]}_{n_\mathrm{t},k,u}$ yields

$$E\left[|\hat{d}^{[s]}_{n_\mathrm{t},k,m} - d^{[s]}_{n_\mathrm{t},k,m}|^2\right] = \frac{1}{M^2}\sum_{u=0}^{M-1} E\left[|D^{[s]}_{n_\mathrm{t},k,u} - \hat{D}^{[s]}_{n_\mathrm{t},k,u}|^2\right] \tag{20}$$

for $m = 0, 1, \ldots, M-1$. With the common assumption that the M data symbols per subcarrier are i.i.d. Gaussian random variables, we note that the outcome of (19) and (20) is completely identical to that of directly performing MMSE estimation of $\{d_{n_\mathrm{t},k,m}\}$ based on the channel observations in the frequency domain. We also note that in some cases it can happen that some of $\{d_{n_\mathrm{t},k,m}\}$ are pre-known, such as the guard symbols (GSs) with zero energy for reducing OOB emission [10]. If the receiver follows the above proposal for low complexity MMSE equalization, the pre-known symbols will still be treated as random variables. Even though exploiting the prior knowledge of the pre-known symbols can improve the MMSE equalization performance, the gain is expected to be marginal due to their small number for the sake of spectral efficiency, not to mention that the gain comes with a considerably increased equalization complexity.

E. MMSE Equalization for FBMC

Even though FBMC has no CP, the soft termination of its filter guarantees multiple near-zero samples at the tail of each FBMC block. By treating the last L_cp samples of the former FBMC block as the CP of the current one, frequency domain equalization becomes feasible. Following the identified link between GFDM and FBMC, we can base on the previous part to analogously perform MMSE equalization for QAM-FBMC. Therefore, this part devotes to the OQAM-FBMC case, considering that the complex-valued multipath fading channel destroys its real-domain orthogonality and we again suffer from ISI, ICI and IAI.

Given the expression in (8), the use of the PHYDYAS filter [9] of length $L_\mathrm{f} = 4K$ yields a OQAM-FBMC block of length $MK + \frac{7}{2}K$. At the receiver, it is convenient to append $K/2$ zeros to the received samples such that we can perform $\tilde{N}$-point DFT, where $\tilde{N} = (M+4)K$ is the smallest integer multiple of K that is greater than the block length. The outcome is

$$\begin{aligned}\tilde{R}_{n_\mathrm{r}}[\nu] &= \sum_{n_\mathrm{t}=1}^{N_\mathrm{t}} H_{n_\mathrm{r},n_\mathrm{t}}[\nu]\tilde{X}_{n_\mathrm{t}}[\nu] + W_{n_\mathrm{r}}[\nu] \qquad (21)\\ &= \sum_{n_\mathrm{t}=1}^{N_\mathrm{t}} H_{n_\mathrm{r},n_\mathrm{t}}[\nu] \\ &\quad\times\left[\sum_{k\in\mathcal{K}} j^k e^{-j\frac{2\pi k}{K}\frac{L_\mathrm{f}-1}{2}} \tilde{G}\left[\left\langle \nu - k\tilde{M}\right\rangle_{\tilde{N}}\right] A_{n_\mathrm{t},k,u=\langle\nu\rangle_{2\tilde{M}}}\right] \\ &\quad + W_{n_\mathrm{r}}[\nu] \qquad (22)\end{aligned}$$

where the second equality is based on (11) and $W_{n_\mathrm{r}}[\nu]$ corresponds to the DFT of the noise samples. Given the similarity between (22) and (17), we can analogously perform MMSE estimation for $\{A_{n_\mathrm{t},k,u}\}$ as the way we did for $\{D_{n_\mathrm{t},k,u}\}$ in the context of GFDM, and then use the results to generate the estimates $\{\hat{a}_{n_\mathrm{t},k,2m}, \hat{a}_{n_\mathrm{t},k,2m+1}\}$ of the real and imaginary parts of the complex data symbols, i.e., (10). Due to the use of OQAM, $\{A_{n_\mathrm{t},k,u}\}$ are DFTs of real rather than complex numbers. Their additional properties as described in (13) shall be considered in the first step. For instance, to estimate $\{A_{n_\mathrm{t},k,u=2}\}$, we shall not only consider the observations at the frequency bins satisfying $\langle\nu\rangle_{2\tilde{M}} = 2$, but also those with $\langle\nu\rangle_{2\tilde{M}} = \tilde{M}-2$ after complex conjugation. The second step is based on the linear mapping

$$\begin{aligned}a_{n_\mathrm{t},k,2m} &= \frac{1}{2\tilde{M}}\sum_{u=0}^{\tilde{M}-1}\left(A_{n_\mathrm{t},k,u} + A_{n_\mathrm{t},k,\tilde{M}+u}\right)e^{j2\pi\frac{2mu}{2\tilde{M}}};\\ a_{n_\mathrm{t},k,2m+1} &= \frac{(-j)(-1)^k}{2\tilde{M}}\sum_{u=0}^{\tilde{M}-1}\left(A_{n_\mathrm{t},k,u} - A_{n_\mathrm{t},k,\tilde{M}+u}\right) \\ &\quad\times e^{j2\pi\frac{(2m+1)u}{2\tilde{M}}}\end{aligned} \tag{23}$$

which is essentially the inverse of (12).

F. Short Summary

Table II lists the arithmetic complexity that is required for MMSE equalization. All waveforms are affected by IAI and the complexity for resolving it scales linearly and quadratically with N_r and N_t, respectively. Even though GFDM and FBMC both are non-orthogonal, their complexity does not scale polynomially with the amount of ICI and ISI. This is because we propose to first estimate the DFTs of the data symbols per subcarrier. In the frequency domain, the amount of ICI is limited by choosing a pulse shaping filter with good frequency localization. And then, a simple IDFT can resolve ISI with the complexity that only grows logarithmically rather than quadratically (as reported in [13], [14]) with the number of data symbols per subcarrier.

IV. Simulation Results

In this section, the waveforms are evaluated in a 4×4 spatial multiplexing MIMO system with spatially uncorrelated multipath Rayleigh fading channels. The metrics of interest include OOB emission, PAPR and coded FER performance. The baseline CP-OFDM is configured as follows: $K = 1536$, $|\mathcal{K}| = 36$, $T = 66.67\mu s$ and $N_\mathrm{s} = 7$. With the subcarrier spacing $T^{-1} = 15\,\mathrm{kHz}$, the occupied subband out of the total 23.04 MHz band has about 0.5 MHz bandwidth. In accordance with Table I, the corresponding configurations for the other waveforms can be computed under the constraint of using the same bandwidth to transmit the same amount of information. Considering the additional degree of freedom in the time domain equipped by GFDM and FBMC, their type-II configuration in Table I is defined by having $M = 12$. Furthermore, UF-OFDM adopts the Dolph-Chebyshev filter with length $L_\mathrm{f} = 74$ and the side-lobe attenuation -51 dB [19]. The filter

TABLE II

MMSE EQUALIZATION ARITHMETIC COMPLEXITY

* The arithmetic complexity is derived from the configurations listed in Table. I and normalized by the number of transmitted data symbols.
* $O(1)$ represents the arithmetic complexity per multiplication.

Waveform	Matched filter	DFT-based processing	Freq. Domain MMSE Equ.
OFDM	–	$O\left(\frac{N_\mathrm{r}}{N_\mathrm{t}}\log K\right)$	$O(N_\mathrm{t}N_\mathrm{r}+N_\mathrm{t}^2)$
F-OFDM	$O\left(\frac{N_\mathrm{r}L_\mathrm{f}(K+L_\mathrm{cp})}{N_\mathrm{t}\lvert\mathcal{K}\rvert}\right)$	$O\left(\frac{N_\mathrm{r}}{N_\mathrm{t}}\log K\right)$	$O(N_\mathrm{t}N_\mathrm{r}+N_\mathrm{t}^2)$
UF-OFDM	–	$O\left(\frac{N_\mathrm{r}}{N_\mathrm{t}}\log(K)\right)$	$O(N_\mathrm{t}N_\mathrm{r}+N_\mathrm{t}^2)$
GFDM-I	–	$O\left(\frac{N_\mathrm{r}}{N_\mathrm{t}}\log(KN_\mathrm{s})+\log(N_\mathrm{s})\right)$	$O(N_\mathrm{t}N_\mathrm{r}+N_\mathrm{t}^2)$
FBMC-I	–	$O\left(\frac{N_\mathrm{r}}{N_\mathrm{t}}\log(N_\mathrm{s}K+4K)+\log(N_\mathrm{s}+4)\right)$	$O(N_\mathrm{t}N_\mathrm{r}+N_\mathrm{t}^2)$
GFDM-II	–	$O\left(\frac{N_\mathrm{r}}{N_\mathrm{t}}\log K+\log M\right)$	$O(N_\mathrm{t}N_\mathrm{r}+N_\mathrm{t}^2)$
FBMC-II	–	$O\left(\frac{N_\mathrm{r}}{N_\mathrm{t}}\log(N_\mathrm{s}K+4K/M)+\log(N_\mathrm{s}M+4)\right)$	$O(N_\mathrm{t}N_\mathrm{r}+N_\mathrm{t}^2)$

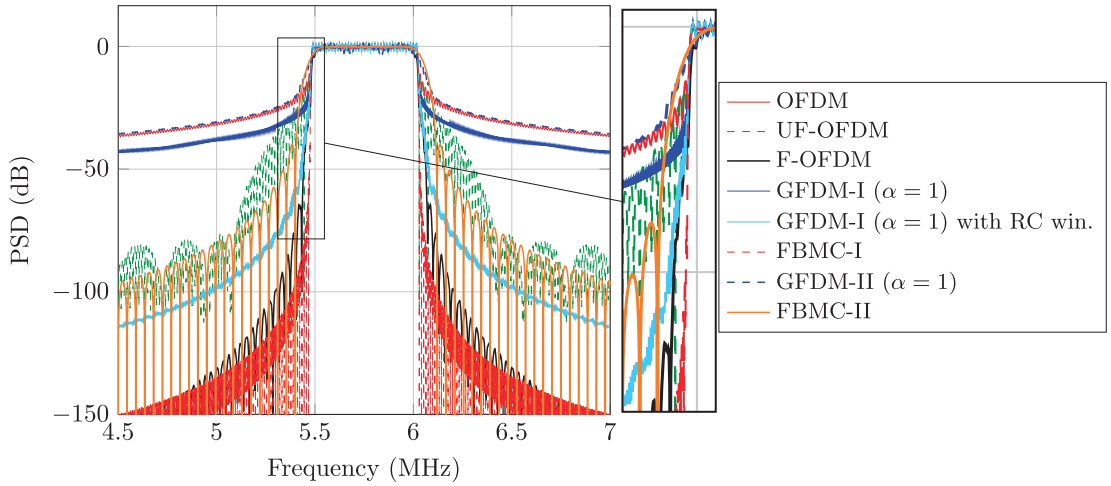

Fig. 3. Power spectral densities (PSDs) of the considered waveforms in their baseband signal form (per transmit antenna), which are MCS irrelevant.

used by F-OFDM is a Hanning windowed sinc-function with length $L_\mathrm{f} = K/2+1$ [18]. The PHYDYAS filter of FBMC has the longest filter length equal to $4K$ [9]. GFDM adopts a periodic RC function with the roll-off factor $\alpha = 1$.[6] On top of the waveforms, two modulation coding schemes (MCSs) are applied. Namely, the turbo code with the generator polynomial $\{1, 15/13\}_o$ can operate at rate $1/2$ and $3/4$,[7] which are respectively modulated with 16 and 64 QAM (gray). Unless otherwise stated, QAM is the default choice. Its comparison with OQAM is always under the same modulation order. We use E_s/N_0 to denote the energy per data symbol to noise ratio.

[6]With $g[n]$ constructed from a real-valued symmetric filter, e.g., RC, an odd M is recommended for GFDM to attain a good condition number of the corresponding modulation matrix [29]. For comparison purpose, GFDM-II however is configured with $M = 12$ to achieve the subcarrier spacing 180 kHz, being identical to the bandwidth of one resource block in LTE. Aiming at a similar condition number with an even M, here we left shift the frequency response of the RC filter by one over $2M$ of the subcarrier spacing and then make the spectrally-shifted RC filter periodic for GFDM-II.

[7]For every six information bits input to the turbo code, we keep all information bits plus two parity bits respectively generated by the two identical component convolutional codes.

A. OOB Emission

Fig. 3 depicts the power spectral density (PSD) of the considered waveforms in their baseband signal form, where the impairment from the RF front-end is not considered. Outside the allocated subband ranging from 5.5 MHz to 6 MHz, the OOB emission of OFDM is very high. This is mainly because the disruptive change from one OFDM block to another in the time domain. Linear filtering is helpful to smoothen the transition between blocks, thereby lower OOB emission being achieved by UF-OFDM, F-OFDM and FBMC. It is worth noting that the longer the filter is, the lower is the achieved OOB emission. For GFDM, one aim of circular filtering is to be confined within each block by tail biting, which unfortunately keeps the disruptive change between blocks. By having longer block duration and reducing the number of blocks per frame, GFDM-I can achieve slightly improved OOB emission performance. However, GFDM-II with the same number of blocks per frame as OFDM achieves nearly identical OOB emission performance. The soft transition of its PSD on the shoulder of the occupied spectrum is due to 1) its wider subcarrier spacing than OFDM; and 2) the large roll-off factor. For the same reasons, such soft transition also appears in the case of FBMC-II.

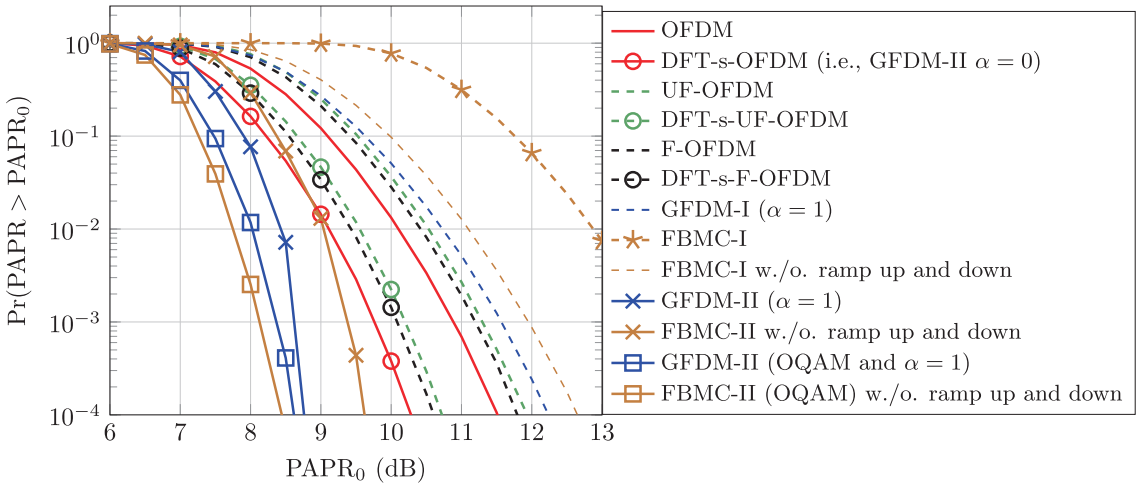

Fig. 4. PAPRs of the considered waveforms in their baseband signal form (per transmit antenna), where the complementary cumulative distribution function is empirically constructed from 10^6 frames and the oversampling factor is 4. The default modulation scheme is 16 QAM (gray). The explicit label *OQAM* represents offset-16 QAM (gray).

Concluding from the above, both OFDM and GFDM require additional techniques for improving their OOB emission performance. Apart from subband-based filtering of F-OFDM and UF-OFDM usable for contiguous subcarrier allocation per user, filtering on a subcarrier basis, as FBMC does, is needed for non-contiguous subcarrier allocation. Compared to linear filtering, time domain windowing can be an attractive solution to reduce the OOB emission of block-based waveforms as well, e.g., in [10], [30], [31]. For instance, GFDM-I uses the minimum time resource among the waveforms, even $6L_{\text{cp}}$ shorter than the baseline OFDM. Being granted with the same time resource as OFDM, we can extend its CP by $3L_{\text{cp}}$ samples and add a cyclic suffix (CS) with identical length. On this basis, we multiply the GFDM block with the frequency domain expression of an RC function, whose ramp up and down are contained by the extended part of the CP and CS. Fig. 3 shows that the OOB emission of GFDM-I with such RC windowing can compete with F-OFDM and FBMC at the frequencies close the edge of the subband. For frequencies distant from the occupied subband, the OOB emission becomes acceptable as well. Besides filtering and windowing, it is also possible to reduce the OOB emission via preprocessing the transmitted data symbols, e.g., [32]–[34]. However, it is beyond the scope of this paper.

B. PAPR

Fig. 4 shows the PAPRs of the considered waveforms. For those using linear filter, we shall note that the ramp up and down of the filtered signal reduce the average power without affecting the peak power. For this reason, we observe the PAPR increment of UF-OFDM, F-OFDM and FBMC-I compared to OFDM. Such increment is particularly large for FBMC due to its long filter length. Since the ramp up and down phase are not critical to the RF front-end, we remove them during the calculation of PAPR, obtaining a much reduced PAPR for FBMC-I as an example.

For GFDM and FBMC, their subcarrier-based filtering plays a role in the achieved PAPR performance. In the type-I configuration, the number of active subcarriers is sufficient such that the main-lobe of their filters determines the PAPR performance. Under the same normalization, their main-lobes have higher peak value than the rectangular window of OFDM, yielding the increased PAPR performance in the type-I configuration. However, exploiting the additional degree of freedom in the time domain, the type-II configuration of both GFDM and FBMC only uses 3 subcarriers by allocating more data symbols per subcarrier. This directly reduces their PAPRs. Furthermore, due to the small number of used subcarriers, the time-domain side-lobes of the adopted filter that add additional signal-superposition effects become the dominant effect. Taking GFDM-II as an example, if we null its roll-off factor, it becomes identical to DFT-s-OFDM, where the spreading factor equals 12. As a well known PAPR reduction technique, it is directly usable for the OFDM-based waveforms. The comparison in Fig. 4 indicates that a non-zero roll-off factor yielding smaller side-lobes of the RC function can further enhance the PAPR of a signal, when being composed of very few number of active subcarriers. Fig. 4 also shows that OQAM is beneficial to further reduce the PAPR of GFDM-II and FBMC-II. If necessary, other PAPR reduction techniques, such as tone reservation and active constellation extension, can be applied on top of these waveforms. However, further discussion on them is beyond the scope of this paper.

C. FER Under a Doubly Dispersive Channel

Even though it is a common practice to derive frequency domain equalization under the assumption of a time-invariant channel during the transmission of each block, it is important to perform performance evaluation under practical continuously time-varying channels. Here, we choose the extended typical urban (ETU) model specified by 3GPP, where the total power of the path gains, averaged over time, is normalized to one. As it exhibits a large delay spread, the long CP in LTE, i.e., $L_{\text{cp}} = 16.67\,\mu$s, is chosen accordingly. Following the Jakes' model, the time variation of the channel is characterized

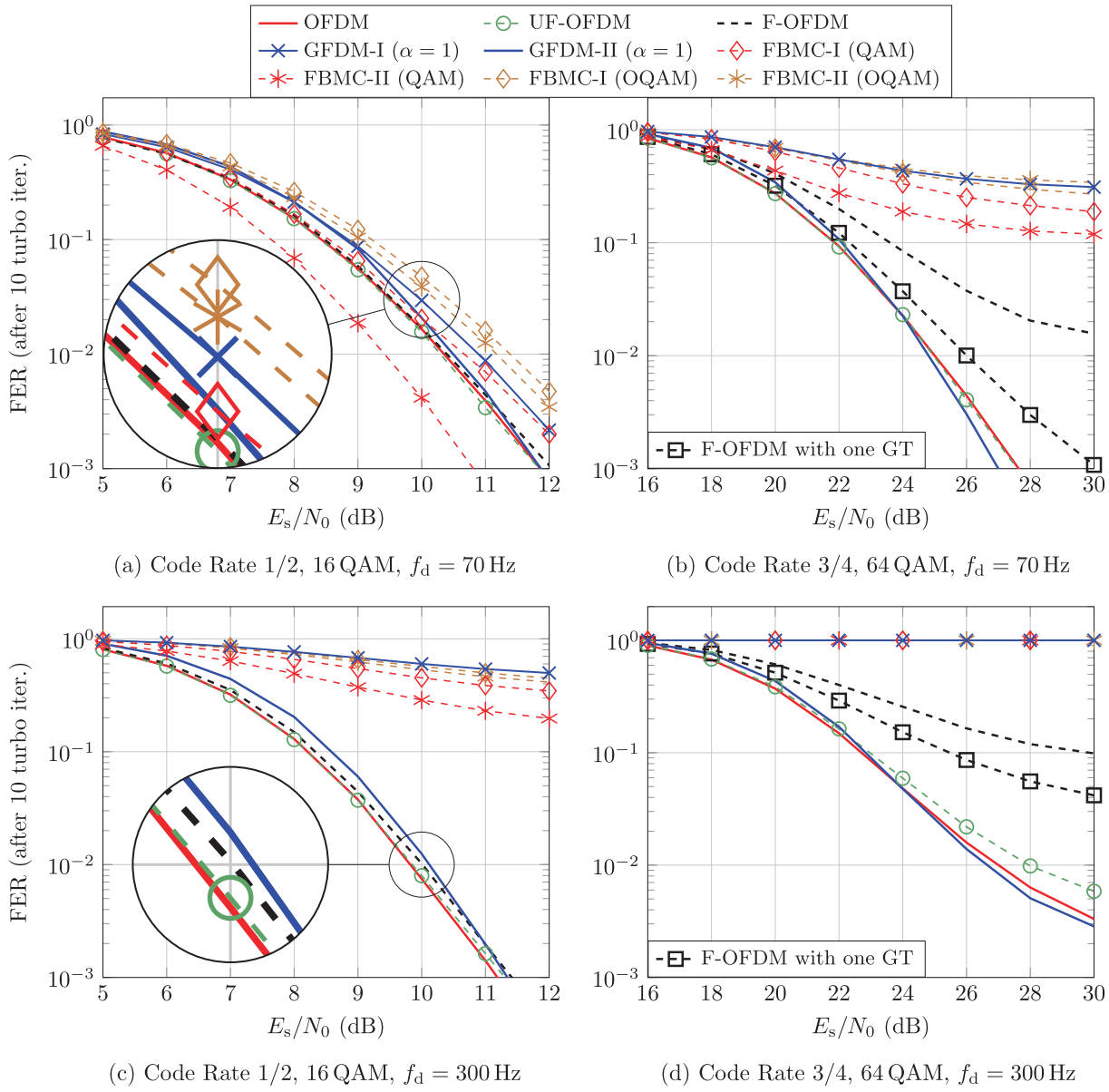

(a) Code Rate 1/2, 16 QAM, $f_d = 70$ Hz

(b) Code Rate 3/4, 64 QAM, $f_d = 70$ Hz

(c) Code Rate 1/2, 16 QAM, $f_d = 300$ Hz

(d) Code Rate 3/4, 64 QAM, $f_d = 300$ Hz

Fig. 5. FERs achieved by the waveforms under perfect synchronization and channel knowledge, where the ETU channel model is considered. With respect to the given 16(64) QAM (gray), the contrastive OQAM configuration is offset-16(64) QAM (gray).

by the maximum Doppler frequency f_d. In this part, the results depicted in Fig. 5 are generated under the assumption of perfect synchronization. Additionally, for coherently equalizing each block, the used CIR is obtained by averaging the true time-variant CIR over the block duration.

In general, the time-varying channel affects the FER performance from two conflicting aspects. First, a changing channel during the transmission of each block introduces ICI [35], which increases along with the maximum Doppler frequency. Second, the time selectivity cross the blocks is desirable for the decoder to exploit the code diversity for an improved decoding performance. When the ICI is comparably smaller than the additive noise, we observe lower FERs at a higher maximum Doppler frequency, e.g., OFDM, UF-OFDM, F-OFDM and GFDM-II in Fig. 5(a) and (c). However, when the operating SNR increases due to the higher MCS, e.g., in Fig. 5(b) and (d), the ICI becomes the dominant factor, degrading the performance as the maximum Doppler frequency increases. For a similar reason, the IBI introduced by linear filtering of UF-OFDM and F-OFDM becomes particularly harmful at the higher MCS. UF-OFDM outperforms F-OFDM as it adopts ZP and shorter filter to ensure limited energy leakage to the subsequent block. In order to improve the performance of F-OFDM, we can either extend the CP or reduce the filter length. As the CP overhead is already 25 %, the latter one is considered here. In the frequency domain, it is equivalent to enlarging the subband by introducing GTs on each side of the subbband. Fig. 5(b) and (d) depict the performance achieved by having one GT on each side of the subband, which costs spectral efficiency, i.e., $(2/38) \approx 5\%$ loss.

Next, we discuss the performance of GFDM and FBMC with their various configurations. GFDM-II is the only one that can achieve performance comparable to or even slightly better than OFDM from the case (a) to (d). Due to circular filtering,

GFDM has no filter tails. Therefore, unlike FBMC, it is not necessary for GFDM to have a long block length for achieving an acceptable temporal efficiency. One critical issue of long blocks is that the time-variant CIR cannot be well approximated by its average value and the resulting mismatched channel knowledge can severely degrade the performance of equalization and subsequent decoding. For this reason, GFDM-I and all configurations of FBMC are not suitable for the maximum Doppler frequency 300 Hz. Even at a lower maximum Doppler frequency 70 Hz, such impairment is non-negligible when the high MCS requires a high operating SNR, i.e., Fig. 5(b). Only in Fig. 5(a), the benefit of FBMC becomes appreciable. This is mainly because its non-orthogonality not only introduces ICI and ISI, but also lets the information of each data symbol be contained by more than one channel observations in the frequency domain. Compared to the type-I configuration, the type-II has larger subcarrier spacing to ensure the necessary frequency selectivity among the channel observations. Furthermore, according to our analysis at the end of Section II-C, QAM can more efficiently exploit the frequency selectivity of the channel than OQAM, therefore outperforming OQAM in Fig. 5. Analogous to FBMC-II, GFDM-II is also equipped with such feature. Between them, FBMC-II in this case has more channel observations per data symbol to achieve a lower FER. However, FBMC-II fails at the higher MCS and/or higher maximum Doppler frequency because the long block length makes it vulnerable under the time-varying channel. On contrary, GFDM-II with its short block length can even slightly outperform OFDM in these cases. In short, (quasi-)orthogonal waveforms, having one channel observation per data symbol, need to resort to coding for exploiting the frequency, time and space selectivity of the channel. While introducing interference, non-orthogonal waveforms permit multiple observations per data symbol to exploit the channel in addition to coding. Therefore, they tend to outperform orthogonal waveforms when the code diversity is deficient, e.g., higher order MCSs.

D. FER With Imperfect Synchronization and Channel Estimation

In this part, we investigate the impact of imperfect synchronization and channel estimation on the performance of the waveforms, where the channel is generated by following another 3GPP channel model termed extended vehicular A model (EVA) with the maximum Doppler frequency equal to 30 Hz and with the sum of the average path gains normalized to one. Due to the reduced maximum delay spread, the CP length accordingly decreases to 4.69 μs (normal mode in LTE).

Starting from channel estimation, we empirically insert a preamble consisting of one baseline CP-OFDM block before each payload frame.[8] Using it, the receiver performs linear MMSE channel estimation by assuming a uniform power-delay profile with maximum delay length equal to L_{cp} [36]. The obtained channel estimates will be used as the true CSI for equalizing the whole frame. This setup assures that the MMSE equalizer of each waveform works with the same quality of channel knowledge. Our primary goal here is to evaluate each waveform with imperfect channel knowledge, rather than to propose a frame structure or an estimation scheme.

Fig. 6(a) shows that FBMC-II and GFDM-II ($\alpha = 1$) both can achieve up to 5 dB gain than the others under imperfect channel knowledge, arising from the estimation error, outdated CSI and Doppler effect. In fact, the channel considered here is less selective in both time and frequency compared to that of Fig. 5(a), but the achieved gains are increased. Before drawing a conclusion from this observation, we experimentally reduce the roll off factor α of GFDM-II from 1 to 0.5 such that its ICI is alleviated. This however reduces the gain. The performance loss of FBMC-II is even bigger after changing from QAM to OQAM. From these additional results, we can come to the point that it is possible to harness the benefits of the waveform-induced interference instead of only suffering from it. To this end, we need good strategies on designing equalization and detection. An over-simplified equalizer that treats the information-bearing interference as background noise will inevitably result in a performance loss in comparison with the (quasi-)orthogonal contenders. With the linear MMSE equalizer developed in this work to jointly tackle the ISI, ICI and IAI, the non-orthogonal waveforms are starting to outperform under challenging channel conditions, e.g., having a large delay spread or with a Doppler spread that not only introduces extra ICI but also degrades the quality of channel estimation, see Fig. 5(a) and Fig. 6(a). The observed gains in both figures may be enlarged if we switch from linear MMSE equalization to more advanced non-linear schemes. This certainly requires further investigation, particularly considering the trade-off between performance and complexity in our future works.

Last but not least, we investigate the sensitivity of the waveforms against symbol time offset (STO) and carrier frequency offset (CFO), respectively. Starting from STO, the use of guard intervals, no matter in the form of CP, ZP with overlap-and-add or soft termination of the filter, provides protection against negative STO estimates, i.e., the estimated frame arrival being earlier than the true one. The performance degradation appears once we have a positive STO estimate. How severe the degradation is depends on the power of the first non-negligible paths of the channel in its discrete-time model.[9] From Fig. 6(b), we can infer that the initial 4 paths of the channel are insignificant. Regarding the CFO, the standards usually specify the oscillator precision tolerance, typically ranging from ± 0.05 ppm to ± 25 ppm. According to Fig. 6(c), the waveforms can work under the CFO up to ± 20 ppm. For FBMC-II and GFDM-II, even with ± 30 ppm CFO, their performances are similar to that of OFDM working with ± 20 ppm CFO.

[8] It consists of N_{t} orthogonal pilot vectors that are periodically modulated onto the subcarriers belonging to the occupied subband plus N_{t} subcarriers on each side for achieving sufficient channel estimation quality also on the edge of the subband.

[9] It is noted that the power-delay profile defines the baseband CIR. Its discrete-time channel model is constructed by sampling the low-pass filtered CIR, where the bandwidth equals the sampling rate [37, Ch. 2]. Therefore, the paths of the power-delay profile may not be identical to those in the discrete-time model.

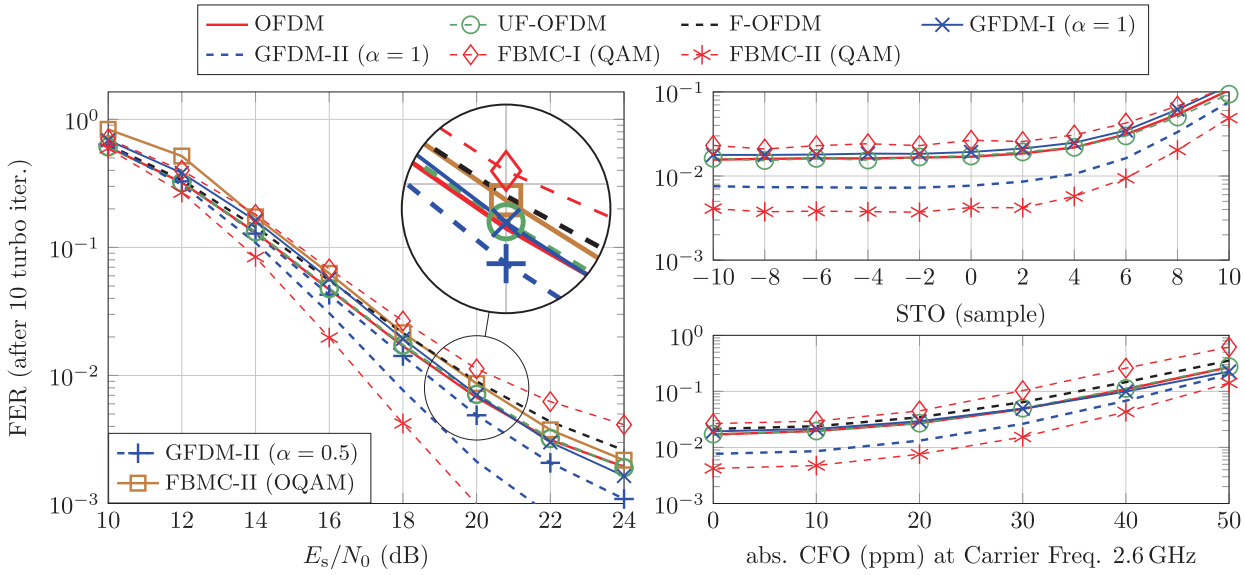

(a) Perf. Sync. and Imperf. Channel Knowledge

(b) Sensitivity to STO and CFO at $E_s/N_0 = 18$ dB and with Imperf. Channel Knowledge

Fig. 6. FERs achieved by the waveforms under the doubly dispersive EVA channel model with the maximum Doppler frequency 30 Hz and relying on imperfect synchronization and channel knowledge, where the 16 QAM (gray) and code rate 1/2 are the default MCS and the contrastive OQAM has the same modulation order, i.e., offset-16 QAM (gray).

V. Conclusion

In this paper, we have analyzed the link level performance of advanced waveforms that are being intensively researched as alternatives to OFDM for future systems. Starting from the two filtered variants of OFDM, both UF-OFDM and F-OFDM can achieve lower OOB emission than OFDM through filtering on a subband basis. Since it is impossible to be time and frequency limited at the same time, lower OOB emission is typically achieved at the cost of time resources. The shorter filter tail of UF-OFDM results in a higher OOB emission compared to F-OFDM. However, the longer filter of F-OFDM introduces more severe IBI. As a consequence, FER degradation is particularly high under rich multipath fading channels and when high order MCSs are in use. They both can achieve similar PAPR performance as OFDM.

We have further investigated more complex waveforms, i.e., GFDM and FBMC. They have two key features. Namely, they are non-orthogonal and have one extra degree of freedom in the time domain, i.e., multiple data symbols per subcarrier are permitted. Their non-orthogonality introduces self-interference, but also offers the possibility to exploit the frequency selectivity of the channel. Together with their second feature, we are able to achieve: 1) lower PAPR performance and 2) better FER under doubly dispersive channels than OFDM and its two variants. Furthermore, we have also investigated the use of QAM and OQAM in combination with them. OQAM was initially introduced to achieve the orthogonality in the real domain, which however cannot be preserved after the complex-valued multipath fading channel. From our analysis, OQAM can offer lower PAPR than QAM, but is not as efficient as QAM in terms of exploiting the frequency selective channel for data transmission. Between GFDM and FBMC, linear filtering of FBMC is beneficial to achieve an ultra-low OOB emission, but requires additional time resources to accommodate the long filter tail. For this reason, it is not an efficient choice for cases that need short block lengths, e.g., fast fading channels. Circular filtering of GFDM on the other hand is an attractive feature for achieving a good comprise in the usage of time and frequency resources. It is worth noting that their non-orthogonality becomes beneficial only if the receiver can effectively resolve the ISI and ICI, plus IAI in MIMO systems. In this paper, we have proposed an implementation of MMSE equalization, which jointly tackles the three dimensional interference with the complexity of the same polynomial order as that of OFDM. As a part of future works, near-optimum receiver designs for them are of interest.

Concluding from the above, in terms of system evolution, F-OFDM and UF-OFDM are straightforward improvements of OFDM and, therefore, they are being considered as a natural choice by 3GPP for intermediary standards or early 5G systems. Nevertheless, non-orthogonal waveforms, i.e. GFDM and FBMC, are definitely worth investigation. We believe their benefits can be exploited with a complexity that is affordable by today's hardware.

Appendix
Markov Chain Based MMSE Equalization for Banded Channel Matrix

Consider a large-scale linear system

$$\mathbf{y} = \mathbf{H}\mathbf{x} + \mathbf{w}, \tag{A.1}$$

where $\mathbf{y} \in \mathbb{C}^{V\times 1}$ is the system output vector obtained from the input vector $\mathbf{x} \in \mathbb{C}^{U\times 1}$, the channel matrix $\mathbf{H} \in \mathbb{C}^{V\times U}$ and

the noise vector $\mathbf{w} \in \mathbb{C}^{V\times 1}$. The likelihood function $p(\mathbf{y}|\mathbf{H},\mathbf{x})$ and the a-priori distribution $p(\mathbf{x})$ are respectively given as

$$p(\mathbf{y}|\mathbf{H},\mathbf{x}) \propto \exp\left(-\frac{\|\mathbf{y}-\mathbf{H}\mathbf{x}\|^2}{\sigma_w^2}\right) = \prod_{v=1}^{V}\exp\left(-\frac{|y_v-\mathbf{h}_v\mathbf{x}|^2}{\sigma_w^2}\right) \quad (A.2)$$

$$p(\mathbf{x}) = \mathcal{CN}(\mathbf{x};\mathbf{0},E_s\mathbf{I}_U), \quad (A.3)$$

where y_v and $\mathbf{h}_v$ are the vth row of $\mathbf{y}$ and $\mathbf{H}$, respectively. By definition, the MMSE estimate of $\mathbf{x}$ equals the mean of $\mathbf{x}$ with respect to $p(\mathbf{x}|\mathbf{y},\mathbf{H})$ [27], which is a Gaussian function.

Consider a band matrix $\mathbf{H}$, e.g.,

$$\mathbf{H} = \begin{bmatrix} h_{11} & h_{12} & h_{13} & \ddots & \ddots \\ 0 & h_{22} & h_{23} & h_{24} & \ddots \\ \vdots & \ddots & h_{33} & h_{34} & h_{35} \end{bmatrix}, \quad (A.4)$$

we can derive a low complexity implementation of MMSE estimation. From the above example, it is easy to notice the position of non-zero entries in $\mathbf{H}$ are shifted from the left-hand side to the right-hand side as the row index grows. Accordingly, we can define a sliding window with length according to the bandwidth of the matrix and shift it from the top to the bottom of the input vector such that only the entries within the window contributing to the output entry at each shift. The feature of sliding window is to drop old samples and get new ones. Between two shifts, there could be some common parts, depending on the step size.

Expressing the above identifications into equations, we introduce the set I_v to collect the column indices of the non-zero entries in $\mathbf{h}_v$. And then, we form two subvectors $\tilde{\mathbf{h}}_v = [\mathbf{h}]_{I_v}$ and $\tilde{\mathbf{x}}_v = [\mathbf{x}]_{I_v}$. The former contains the non-zero entries of $\mathbf{h}_v$. The latter collects the elements residing in the sliding window after v shifts and has the following relation with $\tilde{\mathbf{x}}_{v-1}$

$$\tilde{\mathbf{x}}_v = \mathbf{F}_n\tilde{\mathbf{x}}_{v-1} + [\mathbf{0}^T_{|I_v\cap I_{v-1}|}\,[\mathbf{x}]^T_{I_v\setminus I_{v-1}}]^T \quad (A.5)$$

where the use of the matrix $\mathbf{F}_v \in \{0,1\}^{|I_v|\times|I_{v-1}|}$ is to move the common elements from their former positions in $\tilde{\mathbf{x}}_{v-1}$ to the latter ones in $\tilde{\mathbf{x}}_v$; and $[\mathbf{x}]_{I_v\setminus I_{v-1}}$ are the new entries in $\mathbf{x}$ contributing to the output entry y_v. The Markov property of sliding window further yields

$$p(\tilde{\mathbf{x}}_1,\tilde{\mathbf{x}}_2,\ldots,\tilde{\mathbf{x}}_V) = p(\tilde{\mathbf{x}}_1)\cdot\prod_{v=2}^{V}p(\tilde{\mathbf{x}}_v|\tilde{\mathbf{x}}_{v-1},\ldots,\tilde{\mathbf{x}}_1) = \prod_{v=1}^{V}p(\tilde{\mathbf{x}}_v|\tilde{\mathbf{x}}_{v-1}), \quad (A.6)$$

with $p(\tilde{\mathbf{x}}_1|\tilde{\mathbf{x}}_0) = p(\tilde{\mathbf{x}}_1)$. Together with (A.2), we reach to the following factorization

$$p(\mathbf{y}|\mathbf{H},\mathbf{x})p(\mathbf{x}) = p(\mathbf{y}|\mathbf{H},\tilde{\mathbf{x}})p(\tilde{\mathbf{x}}) = \prod_{v=1}^{V}p(y_v|\mathbf{h}_v,\tilde{\mathbf{x}}_v)p(\tilde{\mathbf{x}}_v|\tilde{\mathbf{x}}_{v-1}) \quad (A.7)$$

which implies

$$p(\tilde{\mathbf{x}}_{v'}|\mathbf{y},\mathbf{H}) \propto \int\prod_{v=1}^{V}p(y_v|\mathbf{h}_v,\tilde{\mathbf{x}}_v)p(\tilde{\mathbf{x}}_v|\tilde{\mathbf{x}}_{v-1})\left[\prod_{\tilde{v}\neq v'}\mathrm{d}\tilde{\mathbf{x}}_{\tilde{v}}\right] = \overrightarrow{\alpha}_{v'}(\tilde{\mathbf{x}}_{v'})\overleftarrow{\beta}_{v'}(\tilde{\mathbf{x}}_{v'}) \quad (A.8)$$

with $\overrightarrow{\alpha}_{v'}(\tilde{\mathbf{x}}_{v'})$ and $\overleftarrow{\beta}_{v'}(\tilde{\mathbf{x}}_{v'})$ defined as

$$\overrightarrow{\alpha}_{v'}(\tilde{\mathbf{x}}_{v'}) = \int\prod_{v=1}^{v'}p(y_v|\mathbf{h}_v,\tilde{\mathbf{x}}_v)p(\tilde{\mathbf{x}}_v|\tilde{\mathbf{x}}_{v-1})\left[\prod_{\tilde{v}=0}^{v'-1}\mathrm{d}\tilde{\mathbf{x}}_{\tilde{v}}\right] \quad (A.9)$$

$$\overleftarrow{\beta}_{v'}(\tilde{\mathbf{x}}_{v'}) = \int\prod_{v=v'+1}^{V}p(y_v|\mathbf{h}_v,\tilde{\mathbf{x}}_v)p(\tilde{\mathbf{x}}_v|\tilde{\mathbf{x}}_{v-1})\left[\prod_{\tilde{v}=v'+1}^{V}\mathrm{d}\tilde{\mathbf{x}}_{\tilde{v}}\right]. \quad (A.10)$$

Equipped with the knowledge of the marginal $p(\tilde{\mathbf{x}}_{v'}|\mathbf{y},\mathbf{H})$, the mean of $\tilde{\mathbf{x}}_v$ with respect to it corresponds to the MMSE estimates of the entries of $\mathbf{x}$ with their indices belonging to I_v. Therefore, MMSE estimation boils down to the computation of $\overrightarrow{\alpha}_{v'}(\tilde{\mathbf{x}}_{v'})$ and $\overleftarrow{\beta}_{v'}(\tilde{\mathbf{x}}_{v'})$.

A. Forward Calculation of $\overrightarrow{\alpha}_v(\tilde{\mathbf{x}}_v)$

From the definition of $\overrightarrow{\alpha}_v(\tilde{\mathbf{x}}_v)$ in (A.9), we can easily identify

$$\overrightarrow{\alpha}_v(\tilde{\mathbf{x}}_v) = p(y_v|\mathbf{h}_v,\tilde{\mathbf{x}}_v)\int\overrightarrow{\alpha}_{v-1}(\tilde{\mathbf{x}}_{v-1})p(\tilde{\mathbf{x}}_v|\mathbf{x}_{v-1})\mathrm{d}\tilde{\mathbf{x}}_{v-1}, \quad (A.11)$$

implying $\{\overrightarrow{\alpha}_v(\tilde{\mathbf{x}}_v)\}$ can be recursively and forwardly computed. Skipping tedious derivations, the function $\alpha_v(\tilde{\mathbf{x}}_v)$ for $v = 1,2,\ldots,V$ is a Gaussian function characterized by the mean $\boldsymbol{\mu}_{\alpha,v}$ and covariance matrix $\boldsymbol{\Sigma}_{\alpha,v}$

$$\boldsymbol{\mu}_{\alpha,v} = \hat{\boldsymbol{\mu}}_{\alpha,v} + \frac{\hat{\boldsymbol{\Sigma}}_{\alpha,v}\tilde{\mathbf{h}}_v^H\left(y_v-\tilde{\mathbf{h}}_v\hat{\boldsymbol{\mu}}_{\alpha,v}\right)}{\tilde{\mathbf{h}}_v\hat{\boldsymbol{\Sigma}}_{\alpha,v}\tilde{\mathbf{h}}_v^H+\sigma_w^2};$$

$$\boldsymbol{\Sigma}_{\alpha,v} = \hat{\boldsymbol{\Sigma}}_{\alpha,v} - \frac{\hat{\boldsymbol{\Sigma}}_{\alpha,v}\tilde{\mathbf{h}}_v^H\tilde{\mathbf{h}}_v\hat{\boldsymbol{\Sigma}}_{\alpha,v}}{\tilde{\mathbf{h}}_v\hat{\boldsymbol{\Sigma}}_{\alpha,v}\tilde{\mathbf{h}}_v^H+\sigma_w^2} \quad (A.12)$$

with $\hat{\boldsymbol{\mu}}_{\alpha,v} = \mathbf{F}_v\boldsymbol{\mu}_{\alpha,v-1}$ and $\hat{\boldsymbol{\Sigma}}_{\alpha,v} = \mathbf{F}_v\boldsymbol{\Sigma}_{\alpha,v-1}\mathbf{F}_v^H + \boldsymbol{\Omega}_v$, where $\boldsymbol{\Omega}_v$ is the covariance matrix of the vector $[\mathbf{0}^T_{|I_v\cap I_{v-1}|}\;[\mathbf{x}]^T_{I_v\setminus I_{v-1}}]^T$ in (A.5). The arithmetic complexity for each update is $O(|I_v|^2)$.

B. Backward Calculation of $\overleftarrow{\beta}_v(\tilde{\mathbf{x}}_v)$

By analogy, the function $\overleftarrow{\beta}_v(\tilde{\mathbf{x}}_v)$ can be recursively computed but in a backward manner

$$\overleftarrow{\beta}_v(\tilde{\mathbf{x}}_v) = \int\overleftarrow{\beta}_{v+1}(\tilde{\mathbf{x}}_{v+1})p(r_{v+1}|\mathbf{h}_{v+1},\tilde{\mathbf{x}}_{v+1})p(\tilde{\mathbf{x}}_{v+1}|\tilde{\mathbf{x}}_v)\mathrm{d}\tilde{\mathbf{x}}_{v+1} \propto \exp\left(-\tilde{\mathbf{x}}_v^H\boldsymbol{\Lambda}_{\beta,v}\tilde{\mathbf{x}}_v + 2\mathrm{Re}\left(\tilde{\mathbf{x}}_v^H\boldsymbol{\Lambda}_{\beta,v}\boldsymbol{\eta}_{\beta,v}\right)\right). \quad (A.13)$$

Fig. 7. Illustration of parallel processing architecture. Instead of computing $\overrightarrow{\alpha}_v(\tilde{\mathbf{x}}_v)$ and $\overleftarrow{\beta}_v(\tilde{\mathbf{x}}_v)$ respectively from the head and tail, we apply a window centered at the target $\tilde{\mathbf{x}}_v$ and start the computation from each boundary of the window at t_0. If applying the window at multiple positions, the results can be simultaneously obtained at the next time instant t_1.

Starting from $\mathbf{\Lambda}_{\beta,v=V} = \mathbf{0}$ and $\mathbf{\Lambda}_{\beta,v}\boldsymbol{\eta}_{\beta,v=V} = \mathbf{0}$, the former $\mathbf{\Lambda}_{\beta,v}$ and $\mathbf{\Lambda}_{\beta,v}\boldsymbol{\eta}_{\beta,v}$ are determined by the knowledge of the latter ones

$$\mathbf{\Lambda}_{\beta,v} = \mathbf{F}_{v+1}^H \left[\left(\mathbf{\Lambda}_{\beta,v+1} + \frac{\tilde{\mathbf{h}}_{v+1}^H \tilde{\mathbf{h}}_{v+1}}{\sigma_w^2} \right) \mathbf{\Omega}_{v+1} + \mathbf{I} \right]^{-1} \times \left(\mathbf{\Lambda}_{\beta,v+1} + \frac{\tilde{\mathbf{h}}_{v+1}^H \tilde{\mathbf{h}}_{v+1}}{\sigma_w^2} \right) \mathbf{F}_{v+1}; \quad \text{(A.14)}$$

$$\mathbf{\Lambda}_{\beta,v}\boldsymbol{\eta}_{\beta,v} = \mathbf{F}_{v+1}^H \left[\left(\mathbf{\Lambda}_{\beta,v+1} + \frac{\tilde{\mathbf{h}}_{v+1}^H \tilde{\mathbf{h}}_{v+1}}{\sigma_w^2} \right) \mathbf{\Omega}_{v+1} + \mathbf{I} \right]^{-1} \times \left[\mathbf{\Lambda}_{\beta,v+1}\boldsymbol{\eta}_{\beta,v+1} + \frac{\tilde{\mathbf{h}}_{v+1}^H}{\sigma_w^2} r_{v+1} \right]. \quad \text{(A.15)}$$

The arithmetic complexity, i.e., $O\left(|I_{v+1} \backslash I_v|^3 + |I_{v+1}|^2\right)$, only scales cubically with the number of new elements between two shifts in the sliding window. With respect to the case of MMSE equalization for GFDM, it has either value zero or N_t.

C. Parallel Processing

Equipped with both $\overrightarrow{\alpha}_v(\tilde{\mathbf{x}}_v)$ and $\overleftarrow{\beta}_v(\tilde{\mathbf{x}}_v)$, we can eventually compute their product for (A.8), which remains to be a Gaussian function parameterized by

$$\boldsymbol{\mu}_{\alpha\beta,v} = \left[\mathbf{I} + \mathbf{\Sigma}_{\alpha,v}\mathbf{\Lambda}_{\beta,v}\right]^{-1} \left[\boldsymbol{\mu}_{\alpha,v} + \mathbf{\Sigma}_{\alpha,v}\mathbf{\Lambda}_{\beta,v}\boldsymbol{\eta}_{\beta,v}\right] \quad \text{(A.16)}$$

$$\mathbf{\Sigma}_{\alpha\beta,v} = \left[\mathbf{I} + \mathbf{\Sigma}_{\alpha,v}\mathbf{\Lambda}_{\beta,v}\right]^{-1} \mathbf{\Sigma}_{\alpha,v}. \quad \text{(A.17)}$$

Straightforwardly, $\boldsymbol{\mu}_{\alpha\beta,v}$ is the MMSE estimate of $\tilde{\mathbf{x}}_v = [\mathbf{x}]_{I_v}$ with the covariance matrix of the estimation error $\mathbf{\Sigma}_{\alpha\beta,v}$. The arithmetic complexity needed for computing them equals $O(|I_v|^3)$. As adjacent subvectors can share many common elements, we only need to save $\overrightarrow{\alpha}_v(\tilde{\mathbf{x}}_v)$ and $\overleftarrow{\beta}_v(\tilde{\mathbf{x}}_v)$ for a selected subset of $\{\tilde{\mathbf{x}}_v\}_{v=1,2,...,V}$, and then compute the their product to obtain the MMSE estimates of all entries in $\mathbf{x}$. We should choose such a subset with the smallest size for complexity saving. In general, the complexity of MMSE equalization for a banded matrix grows cubically with the bandwidth of the matrix and only linearly with the output dimension U.

Since $\overrightarrow{\alpha}_v(\tilde{\mathbf{x}}_v)$ and $\overleftarrow{\beta}_v(\tilde{\mathbf{x}}_v)$ both need to be recursively computed, the processing latency can be a concern. Here, due to the Markov property, the dependency between $\tilde{\mathbf{x}}_v$ and $\tilde{\mathbf{x}}_{v'}$ conditional on $(\mathbf{y}, \mathbf{H})$ tends to decrease as the difference $|v - v'|$ increases. Therefore, we can conduct parallel processing without comprising the accuracy, see Fig. 7. This technique has been successfully applied for decoding convolutional codes, which also exhibit the Markov property [38].

ACKNOWLEDGEMENTS

The computations were performed on a computing cluster at the Center for Information Services and High Performance Computing (ZIH), TU Dresden.

REFERENCES

[1] R. Hattachi *et al.* NGMN. (Feb. 2015). *5G White Paper*. [Online]. Available: https://www.ngmn.org/5g-white-paper.html
[2] G. P. Fettweis, "The tactile Internet: Applications and challenges," *IEEE Veh. Technol. Mag.*, vol. 9, no. 1, pp. 64–70, Mar. 2014.
[3] N. Tadayon and S. Aissa, "Modeling and analysis of cognitive radio based IEEE 802.22 wireless regional area networks," *IEEE Trans. Wireless Commun.*, vol. 12, no. 9, pp. 4363–4375, Sep. 2013.
[4] P. Banelli, S. Buzzi, G. Colavolpe, A. Modenini, F. Rusek, and A. Ugolini, "Modulation formats and waveforms for 5G networks: Who will be the heir of OFDM?: An overview of alternative modulation schemes for improved spectral efficiency," *IEEE Signal Process. Mag.*, vol. 31, no. 6, pp. 80–93, Nov. 2014.
[5] L. B. Le *et al.*, "Enabling 5G mobile wireless technologies," *EURASIP J. Wireless Commun. Netw.*, vol. 2015, p. 218, Dec. 2015.
[6] G. Wunder *et al.*, "5GNOW: Non-orthogonal, asynchronous waveforms for future mobile applications," *IEEE Commun. Mag.*, vol. 52, no. 2, pp. 97–105, Feb. 2014.
[7] X. Zhang *et al.*, "Filtered-OFDM—Enabler for flexible waveform in the 5th generation cellular networks," in *Proc. IEEE Global Telecommun. Conf. (GLOBECOM)*, San Diego, CA, USA, Dec. 2015, pp. 1–6.
[8] T. Wild, F. Schaich, and Y. Chen, "5G air interface design based on universal filtered (UF-)OFDM," in *Proc. IEEE Int. Conf. on Digital Signal Process. (DSP)*, Hong Kong, China, Aug. 2014, pp. 699–704.
[9] M. Bellanger *et al.,* "FBMC physical layer: a primer," in PHYDYAS project, Jan. 2010. [Online]. Available: http://ict-phydyas.org
[10] N. Michailow *et al.*, "Generalized frequency division multiplexing for 5th generation cellular networks," *IEEE Trans. Commun.*, vol. 62, no. 9, pp. 3045–3061, Sep. 2014.
[11] A. Aminjavaheri *et al.*, "Impact of timing and frequency offsets on multicarrier waveform candidates for 5G," in *Proc. IEEE Signal Process. Signal Process. Edu. Workshop (SP/SPE)*, Salt Lake City, Utah, USA, Aug. 2015, pp. 178–183.
[12] T. Ihalainen *et al.*, "Channel equalization for multi-antenna FBMC/OQAM receivers," *IEEE Trans. Veh. Technol.*, vol. 60, no. 5, pp. 2070–2085, Jun. 2011.
[13] M. Matthe, I. Gaspar, D. Zhang, and G. Fettweis, "Reduced complexity calculation of LMMSE filter coefficients for GFDM," in *Proc. IEEE Veh. Technol. Conf., (VTC) Fall*, Boston, MA, USA, Sep. 2015, pp. 1–2.
[14] A. Farhang *et al.*, "Low complexity GFDM receiver design: A new approach," in *Proc. IEEE Int. Conf. Commun. (ICC)*, London, U.K., Jun. 2015, pp. 4775–4780.
[15] W. Jiang and M. Schellmann, "Suppressing the out-of-band power radiation in multi-carrier systems: A comparative study," in *Proc. IEEE Global Telecommun. Conf. (GLOBECOM)*, Anaheim, CA, USA, Sep. 2012, pp. 1477–1482.
[16] J. Bazzi, P. Weitkemper, K. Kusume, A. Benjebbour, and Y. Kishiyama, "Design and performance tradeoffs of alternative multi-carrier waveforms for 5G," in *Proc. IEEE Globecom Workshops (GC Wkshps)*, Dec. 2015, pp. 1–6.
[17] N. E. Tunali, M. Wu, C. Dick, and C. Studer, "Linear large-scale MIMO data detection for 5G multi-carrier waveform candidates," in *Proc. Asilomar Conf. Signals, Syst., Comput.*, Pacific Grove, CA, USA, Jun. 2015, pp. 1–5.

[18] J. Abdoli, M. Jia, and J. Ma, "Filtered OFDM: A new waveform for future wireless systems," in *Proc. IEEE Int. Workshop Signal Process. Adv. Wireless Commun. (SPAWC)*, Stockholm, Sweden, Jun. 2015, pp. 66–70.

[19] M. Matthe, D. Zhang, F. Schaich, T. Wild, R. Ahmed, and G. Fettweis, "A reduced complexity time-domain transmitter for UF-OFDM," in *Proc. IEEE Veh. Technol. Conf. (VTC Spring)*, Nanjing, China, May 2016, pp. 1–5.

[20] F. Schaich, T. Wild, and Y. Chen, "Waveform contenders for 5G—Suitability for short packet and low latency transmissions," in *Proc. IEEE Veh. Technol. Conf. (VTC Spring)*, Seoul, South Korea, May 2014, pp. 1–5.

[21] B. Farhang-Boroujeny, "OFDM Versus Filter Bank Multicarrier," *IEEE Signal Process. Mag.*, vol. 28, no. 3, pp. 92–112, May 2011.

[22] H. Lin and P. Siohan, "An advanced multi-carrier modulation for future radio systems," in *Proc. IEEE Int. Conf. Acoust., Speech Signal Process. (ICASSP)*, Florence, Italy, May 2014, pp. 8097–8101.

[23] A. RezazadehReyhani, A. Farhang, and B. Farhang-Boroujeny, "Circularly pulse-shaped waveforms for 5G: Options and comparisons," in *Proc. IEEE Global Commun. Conf. (GLOBECOM)*, San Diego, CA, USA, Dec. 2015, pp. 1–7.

[24] A. Farhang, N. Marchetti, and L. E. Doyle, "Low-complexity modem design for GFDM," *IEEE Trans. Signal Process.*, vol. 64, no. 6, pp. 1507–1518, Mar. 2016.

[25] P. Siohan, C. Siclet, and N. Lacaille, "Analysis and design of OFDM/OQAM systems based on filterbank theory," *IEEE Trans. Signal Process.*, vol. 50, no. 5, pp. 1170–1183, May 2002.

[26] C. Studer, S. Fateh, and D. Seethaler, "ASIC implementation of soft-input soft-output MIMO detection using MMSE parallel interference cancellation," *IEEE J. Solid-State Circuits*, vol. 46, no. 7, pp. 1754–1765, Jul. 2011.

[27] S. M. Kay, "Fundamentals of statistical signal processing," *Estimation Theory*, vol. 1. Englewood Cliffs, NJ, USA: Prentice-Hall, 1993.

[28] B. Muquet, M. de Courville, P. Duhamel, G. B. Giannakis, and P. Magniez, "Turbo demodulation of zero-padded OFDM transmissions," *IEEE Trans. Commun.*, vol. 50, no. 11, pp. 1725–1728, Nov. 2002.

[29] M. Matthe, L. L. Mendes, and G. Fettweis, "Generalized frequency division multiplexing in a Gabor transform setting," *IEEE Commun. Lett.*, vol. 18, no. 8, pp. 1379–1382, Aug. 2014.

[30] H. Lin and P. Siohan, "Multi-carrier modulation analysis and WCP-COQAM proposal," *EURASIP J. Adv. Signal Process.*, vol. 2014, no. 1, pp. 1–79, 2014.

[31] B. Farhang-Boroujeny, A. Farhang, A. RezazadehReyhani, A. Aminjavaheri, and D. Qu, "A comparison of linear FBMC and circularly shaped waveforms," in *Proc. IEEE Int. Conf. Wireless Inf. Technol. Syst. (ICWITS) Appl. Comput. Electromagn. (ACES)*, Honolulu, Hawaii, USA, Mar. 2016, pp. 1–2.

[32] J. V. D. Beek and F. Berggren, "N-continuous OFDM," *IEEE Commun. Lett.*, vol. 13, no. 1, pp. 1–3, Jan. 2009.

[33] Z. Yuan and A. M. Wyglinski, "On sidelobe suppression for multicarrier-based transmission in dynamic spectrum access networks," *IEEE Trans. Veh. Technol.*, vol. 59, no. 4, pp. 1998–2006, May 2010.

[34] P. Kryszkiewicz and H. Bogucka, "Out-of-band power reduction in NC-OFDM with optimized cancellation carriers selection," *IEEE Commun. Lett.*, vol. 17, no. 10, pp. 1901–1904, Oct. 2013.

[35] Y. Mostofi and D. C. Cox, "ICI mitigation for pilot-aided OFDM mobile systems," *IEEE Trans. Wireless Commun.*, vol. 4, no. 2, pp. 765–774, Mar. 2005.

[36] Y. Li, L. J. Cimini, and N. R. Sollenberger, "Robust channel estimation for OFDM systems with rapid dispersive fading channels," *IEEE Trans. Commun.*, vol. 46, no. 7, pp. 902–915, Jul. 1998.

[37] D. Tse and P. Viswanath, *Fundamentals of Wireless Communication*. New York, NY, USA: Cambridge Univ. Press, 2005.

[38] C. Schurgers, F. Catthoor, and M. Engels, "Memory optimization of MAP turbo decoder algorithms," *IEEE Trans. Very Large Scale Integr. (VLSI) Syst.*, vol. 9, no. 2, pp. 305–312, Apr. 2001.

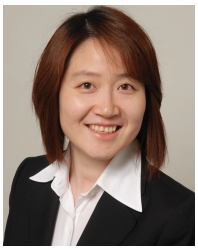

Dan Zhang received the B.Sc. degree in electrical engineering from Zhejiang University, China, in 2004, the M.Sc. and Dr.-Ing. degrees in electrical engineering and information technology from RWTH Aachen University, Aachen, Germany, in 2007 and 2013, respectively, the Ph.D. degree, with a focus on iterative receiver designs. Since 2014, she has been a Post-Doctoral Researcher with Vodafone Chair Mobile Communications Systems, Technische Universität Dresden. She has worked on various national and international research projects with publication in journals, conference proceedings, and workshops. Her current research interests include large-scale statistical inference problems, communication theory, near-optimal transceiver design for 5G, statistical signal processing, communication theory, and optimization theory.

Maximilian Matthé received the Dipl.-Ing degree in electrical engineering from Technische Universität Dresden, Dresden, Germany, in 2013, where he is currently pursuing the Ph.D. with the Vodafone Chair Mobile Communication Systems. His Diploma thesis was focused on waveform design for flexible multicarrier transmission systems. During his studies, he focused on mobile communications systems and communication theory. He performed his internship with National Instruments Dresden and was involved in the design and implementation of a measurement site for LTE test UEs. His research focuses on the design and evaluation of MIMO architectures for future cellular networks.

Luciano Leonel Mendes received the B.Sc. and M.Sc. degrees in electrical engineering from Inatel, Brazil, in 2001 and 2003, respectively, and the Doctor degree in electrical engineering from Unicamp, Brazil, in 2007. He was a Post-Doc Visiting Researcher, sponsored by CNPq-Brasil, Vodafone Chair Mobile Communications Systems, Technische Universität Dresden, from 2013 until 2015. Since 2001, he has been a Professor with the Instituto Nacional de Telecomunicações (Inatel), where he has acted as the Technical Manager of the Hardware Development Laboratory from 2006 to 2012. He has coordinated the Master Program with Inatel and several research projects funded by FAPEMIG, FINEP, and BNDES. His main area of research is wireless communication, multicarrier modulations for 5G networks, and future mobile communications systems.

Gerhard P. Fettweis (F'09) received the Ph.D. degree from RWTH Aachen, Germany, in 1990. He was with IBM Research and then with TCSI Inc., USA. Since 1994, he has been the Vodafone Chair Professor with Technische Universität Dresden, Dresden, Germany. His main research interest on wireless transmission and chip design. He holds an honorary doctorate with the Tampere University of Technology. As a repeat entrepreneur he has cofounded 11 startups so far. He has setup funded projects close to 1/2 billion euros in size. Notably, he runs the German Science Foundation's CRC HAEC and COE cfAED. He is actively involved in organizing IEEE conferences. He was the TPC Chair of the ICC in 2009 and the TTM in 2012, and the General Chair of the VTC Spring in 2013, and the DATE in 2014.